Results in Engineering 30 (2026) 111168

Contents lists available at ScienceDirect

Results in Engineering

journal homepage: www.sciencedirect.com/journal/results-in-engineering

Research paper

Smith chart–based impedance matching and chirality analysis of an ultra-broadband plasmonic graphene absorber for sensing applications

Nastaran Korani [a], Saeed Mohammadi [a], Abdesselam Hocini [b], Mohammad Danaie [a,*]

[a] Faculty of Electrical and Computer Engineering, Semnan University, Semnan, Iran
[b] University of M'sila, Université de M'sila, Algeria

ARTICLE INFO

Keywords:
Broadband absorber
Surface plasmons
Graphene
Perturbation
Smith chart

ABSTRACT

In this work, a graphene-based optical absorber is proposed, with the primary objective of achieving a comprehensive design and performance evaluation of a terahertz (THz) metamaterial absorber. The proposed structure demonstrates ultra-broadband absorption characteristics along with dynamic tunability, achieved through modulation of the graphene Fermi energy. The physical mechanism underlying this broadband response is systematically investigated and is attributed to the synergistic excitation of surface plasmon polaritons (SPP) resonances induced by localized surface charge distributions on the graphene strips and disks. To enable accurate analysis within the subwavelength regime, analytical expressions for the surface current density on the graphene elements are rigorously derived using perturbation theory under normally incident plane-wave excitation. Furthermore, the results obtained from full-wave electromagnetic simulations are quantitatively validated through comparison with those derived from an equivalent circuit model. For this purpose, an equivalent circuit representation consisting of six lumped elements is developed. The optimal values of the resistive, inductive, and capacitive components are determined using a dedicated cost function, resulting in a low Sum of Squared Errors (SSE) of 1.573, which indicates excellent agreement between the models. In addition to its absorption functionality, the proposed structure exhibits strong potential for refractive index sensing over a broad spectral range. The sensing performance is evaluated, demonstrating a high sensitivity of 3.3 THz/RIU. Comprehensive numerical investigations confirm the effectiveness and robustness of the proposed absorber, highlighting its suitability for a wide range of THz applications, including sensing, high-resolution imaging, and secure communication systems.

1. Introduction

Artificially engineered materials, commonly referred to as metamaterials (MMs), have emerged as a prominent focus of scientific research owing to their extraordinary electromagnetic properties that are not observed in naturally occurring media. These structured materials, composed of subwavelength unit cells significantly smaller than the wavelength of the incident radiation, enable unprecedented control over electromagnetic wave propagation. Notable phenomena exhibited by MMs include negative refractive index [1], negative electrical permittivity [2], and the theoretical possibility of achieving electromagnetic cloaking or invisibility [3]. Metamaterials have been extensively investigated and experimentally realized across a wide range of frequency regimes, spanning from the terahertz (THz) domain [4] and infrared spectrum [5–7] to the visible range [8–10]. In particular, the development of Metamaterial Perfect Absorbers (MMPAs) [11–17] has largely leveraged these unconventional electromagnetic responses, especially negative refractive index characteristics. The rapid evolution of modern telecommunication systems and electronic technologies has significantly increased the demand for high-frequency components, such as power dividers [18–23], filters [24–26], sensors [27–29], antennas [30], and electromagnetic absorbers [31–37]. Although early designs of perfect absorbers, including the seminal work by Landi et al., [38], demonstrated high absorption efficiency, they were generally limited by a lack of tunability and reconfigurability in their operational characteristics.

Graphene, a monolayer of carbon atoms arranged in a two-dimensional hexagonal honeycomb lattice [39,40], has emerged as a highly promising material for advanced photonic and electronic applications. It exhibits exceptional electrical and optical properties,

* Corresponding author.
E-mail address: danaie@semnan.ac.ir (M. Danaie).

https://doi.org/10.1016/j.rineng.2026.111168
Received 24 February 2026; Received in revised form 16 May 2026; Accepted 19 May 2026
Available online 20 May 2026

including the quantum Hall effect [41], gate-tunable optical conductivity [42], tunable plasmonic behavior [43], and ultrafast carrier dynamics [44,45]. One of the most significant features of graphene is its ability to support surface plasmon polaritons (SPPs), particularly in the terahertz (THz) frequency regime, which makes it an attractive platform for THz wave absorption applications. In doped graphene, pronounced plasmonic characteristics arise, where the plasmon resonance frequency can be dynamically controlled through external electrical biasing. Moreover, graphene supports SPP propagation in both the THz and infrared regions with substantially longer propagation lengths compared to conventional noble metals, thereby offering reduced losses and enhanced device performance.

Plasmonics has emerged as a rapidly advancing field within nanophotonics, primarily concerned with the interaction of electromagnetic waves with nanostructured materials at subwavelength scales. The ability to confine and guide electromagnetic energy in such structures has enabled the development of a wide range of integrated photonic components, including filters [46–48], switches [49–51], and sensors [52–54]. Graphene-based absorbers, in particular, offer several advantages, among which dynamic tunability is the most prominent. These absorbers can be broadly classified into solar absorbers [55,56] and terahertz absorbers [57,58], depending on their operational frequency range. Furthermore, based on their spectral characteristics, graphene absorbers are categorized as either narrowband [59,60] or broadband [61–63]. Conventional approaches to achieving tunability, such as the integration of PIN diodes [64,65] or the use of micro-electro-mechanical systems (MEMS) [66], often introduce significant fabrication complexity and increased system cost. In contrast, the incorporation of graphene into the absorber architecture provides a more efficient and compact solution for achieving dynamic reconfigurability. By externally modulating the chemical potential (i.e., the Fermi level) of graphene, both the absorption efficiency and resonance frequency can be continuously tuned over a wide frequency range without necessitating any physical alteration of the device structure. The performance of the proposed structure is rigorously analyzed using the finite-difference time-domain method (FDTD) technique [67], ensuring accurate characterization of its electromagnetic response.

Recently, several advanced designs for graphene-based THz absorbers have been proposed, focusing on broadband absorption and sensing capabilities [68–71]. Broadband absorbers are increasingly vital in advanced sensing technologies thanks to their ability to maintain high sensitivity and selectivity over extended spectral ranges [72–75]. In this study, we propose and numerically analyze a multilayer graphene-based broadband absorber capable of delivering near-total absorption across a wide terahertz band.

2. Optical absorbers

Graphene, a two-dimensional material with atomic-scale thickness, is capable of supporting surface plasmon polaritons (SPPs) in the terahertz (THz) frequency regime [76]. It exhibits a range of exceptional physical and electromagnetic properties, including tunable surface conductivity and the ability to sustain low-loss SPP propagation at THz frequencies. A particularly significant feature of graphene is its electrically and magnetically tunable conductivity, which facilitates the development of reconfigurable electronic and photonic devices. This tunability is especially advantageous in the THz domain, where the sign change in the imaginary part of graphene's surface conductivity [77] plays a critical role in enabling controllable plasmonic behavior and dynamic modulation of device response.

Surface Plasmon Polaritons (SPPs) refer to electromagnetic waves that propagate along the interface separating a metal and a dielectric medium. The term SPP explicitly signifies that the wave involves both charge oscillation within the metal termed the surface plasmon and the electromagnetic wave propagation within the dielectric known as the polariton [78]. SPPs fundamentally represent confined guided modes capable of propagating within plasmonic nanostructures. For SPPs to be successfully excited at the metal dielectric boundary, an incident photon must satisfy two critical conditions: its frequency must match the SPP resonant frequency, and its parallel wave vector component (k_x or $k_{||}$) along the interface must be precisely equal to the SPP propagation constant [79].

The proposed device architecture consists of a reflective gold ground plane, followed by a silicon dioxide (SiO_2) dielectric spacer, an array of periodic graphene ribbons, a second SiO_2 dielectric layer, and a patterned graphene top layer composed of periodic graphene disks. This hybrid multilayer configuration is carefully engineered to support strong and overlapping plasmonic resonances, thereby enabling broadband and spectrally stable absorption performance across a wide frequency range. Beyond its broadband absorption characteristics, a key application of the proposed structure lies in refractive index sensing. The sensing mechanism is based on the spectral shift of the absorption peaks induced by variations in the refractive index of the material under test (MUT). This approach provides high sensitivity while benefiting from the inherently broad operational bandwidth of the absorber, enabling multi-frequency sensing with improved robustness and accuracy. Initially, the geometric parameters of the structure are optimized to maximize absorption efficiency. Subsequently, electromagnetic field distributions are analyzed to clarify the underlying physical mechanisms responsible for the observed absorption behavior. In addition, equivalent circuit theory is employed to validate the full-wave simulation results. Finally, the sensing performance of the proposed design is systematically evaluated, demonstrating its potential for refractive index detection applications. Overall, the results suggest a promising route toward the development of advanced and practical terahertz active components.

3. Analytical model and the proposed structure

This section introduces an analytical equivalent circuit model specifically tailored for the two-dimensional arrays comprising both graphene disks and strips. Initially, we derive analytical expressions for the surface current density on these graphene strips and disks within the sub-wavelength regime. This derivation employs perturbation theory, by assuming a normally incident plane wave. Subsequently, the derived RLC equivalent circuit is presented. Leveraging these analytical concepts, a specific dual-layer graphene THz absorber has been conceived and computationally simulated. As illustrated in Fig. 1(a), the unit cell of this structure functions as a broadband, two-layer absorber. The bottom layer consists of a gold film with a thickness of t, which acts as a perfect reflector. This reflection mechanism effectively drives the transmittance to zero, thereby facilitating optimal absorption. Resting atop the reflector is a dielectric spacer layer composed of SiO_2 with a thickness of d_1. This layer is crucial for achieving impedance matching between the free space and the structure. The uppermost layer features an alternating pattern of graphene strips. Graphene, being a zero-bandgap material, necessitates bandgap engineering for its effective utilization in electronic devices such as absorbers.

One established methodology for opening this inherent bandgap involves electron confinement. By patterning a graphene sheet into graphene nanoribbons, electron movement is restricted along one dimension, thereby inducing a finite bandgap in the graphene structure. The opening of this energy bandgap through the transformation of graphene into graphene nanoribbons is scientifically facile and can be readily achieved using standard lithographic techniques [80].

The width of these ribbons is denoted by w, and their periodic spacing by D. In the design of this structure, it is assumed that the graphene ribbons possess infinite length along the y-direction. For the graphene strips incorporated into the structure, an incident TM-polarized wave strikes them perpendicularly. This normal incidence results in the induction of a surface current density exclusively in the x-direction across the ribbon, since the electric field component of the

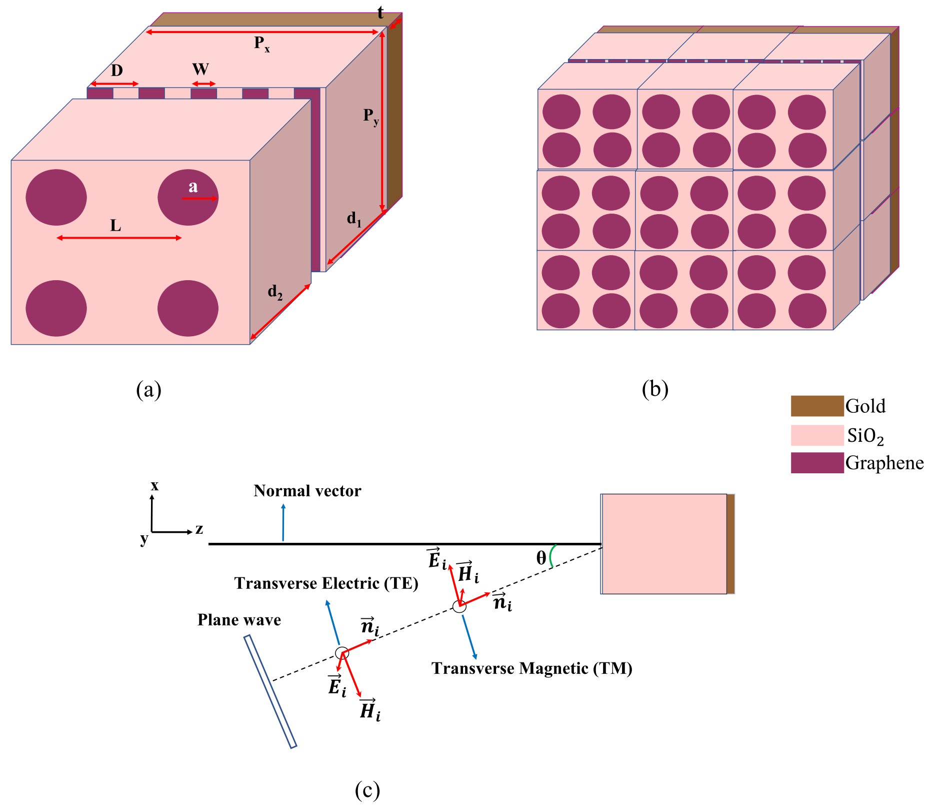

Fig. 1. (a) The unit cell of the proposed absorber. (b) The schematic representation of the proposed absorber. (c) TE and TM modes concept for an incident wave on proposed absorber.

incident radiation is oriented along x. When the wave interacts with the strip, a Surface Plasmon Polariton (SPP) is excited within the ribbon, propagating along the x-axis. These propagating SPPs undergo phase retardation as they reflect off the edges of the finite-length strips. If the total phase shift accumulated by the plasmonic mode upon reflection is an integer multiple of 2π, constructive interference occurs, resulting in a sharp resonance.

While the primary absorption spectra and field distributions in this study are obtained through rigorous full-wave numerical simulations, relying solely on numerical black-box computations is insufficient for a deep physical understanding. Therefore, the following analytical formulations, which include the Kubo model for graphene conductivity, effective medium theory for impedance matching, and equivalent circuit modeling, are herein presented. These mathematical models are actively utilized in the subsequent sections to decode the underlying physical mechanisms of the numerical results. They serve to analytically prove the conditions for near-perfect THz absorption, explain the tunability mechanisms, and rigorously validate the accuracy of the numerical simulations through comparative analytical-numerical analysis.

The resonance frequency can then be determined by the following relationship:

$$2\omega\beta_p + 2\theta = 2n\pi,\ n = 1, 2, \ldots \tag{1}$$

where β_p is the propagation constant of the plasmonic mode and θ is the phase shift resulting from the reflections at the ribbon edges. Since the incident wave is polarized along the x-direction, the surface current density, $J_x(x)$, at any point on the graphene ribbon is governed by the two-dimensional Ohm's law, in which the total electric field comprises the external incident field and the field induced by the surface charges [81]:

$$\frac{J_x(x)}{\sigma_s} = E_x^{ext}(x) + E_x^{\rho}(x) \tag{2}$$

In this relation, $E_x^{ext}(x)$ is the external electric field and $E_x^{\rho}(x)$ is the electric field induced by the accumulated surface charges ρ_s on the graphene. The surface charge density is linked to the current density via the continuity equation for electric charge ($\rho_s = (j\omega)^{-1} \mathrm{d}J_x/\mathrm{d}x$). As this surface charge density is solely a function of x, the resulting induced electric field can therefore, be readily calculated under the quasi-static approximation. By computing this induced field and substituting it into Eq. (2), and subsequently multiplying both sides of the rearranged equation by $2j\omega\varepsilon_0$, we obtain the following governing relationship [82]:

$$\beta_p J_x(x) = 2j\omega\varepsilon_0 E_x^{ext}(x) + \frac{1}{\pi} P \int_{-w/2}^{w/2} \frac{1}{x - x'} \frac{\mathrm{d}J_x(x')}{dx'} dx' \tag{3}$$

The integral relationship incorporates the symbol P, which signifies the Cauchy Principal Value integration. The solution domain is constrained by the physical requirement that the current density must vanish at the ribbon boundaries, providing the essential boundary condition for the system: $J_x(-w/2) = J_x(w/2) = 0$. To analytically solve Eq. (3), we transform the problem into its associated eigenvalue representation [83]:

$$\frac{1}{\pi} P \int_{-w/2}^{w/2} \frac{1}{x - x'} \frac{\mathrm{d}\psi_n(x')}{dx'} dx' = k_n \psi_n(x) \tag{4}$$

In this formulation, ψ_n represents the n-th normalized eigenfunction, satisfying the orthogonality condition $\int_{-w/2}^{w/2} \psi_n^2(x) dx = 1$, and k_n is the corresponding eigenvalue. The solutions obtained from Eq. (4) are interpreted as the fundamental eigenmodes of the graphene ribbon structure. The methodology for obtaining the analytical solutions for this equation, specifically by employing a Fourier series expansion technique applied to the eigenfunctions, has been thoroughly detailed in previous literature [84]. Table 1 is dedicated to presenting the characteristics of the first three plasmonic eigenmodes, specifically summarizing the associated eigenvalues and their corresponding eigenfunction profiles.

The current density across the ribbons can be expanded over the strip modes as follows.

$$J_x(x) = \sum_{n=1}^{\infty} A_n \psi_n(x) \tag{5}$$

By substituting Eq. (5) into Eq. (3) and leveraging the orthogonality of ψ_n, we have:

$$A_n = \frac{2j\omega\varepsilon_{eff}}{\beta_p(\omega) - k_n} - \int_{\frac{w}{2}}^{\frac{w}{2}} E_x^{ext}(x)\psi_n(x)dx \tag{6}$$

Assuming a graphene sheet embedded between two dielectric media with permittivities ε_1 and ε_2, and noting that both the upper and lower dielectrics are SiO_2, the effective permittivity can be expressed as $\varepsilon_{eff} = \frac{\varepsilon_0(\varepsilon_1+\varepsilon_2)}{2} = \varepsilon_0\varepsilon_1$.

Above the graphene layer, an additional SiO_2 dielectric layer with a thickness of d_2 is introduced. This layer serves a pivotal role in achieving impedance matching within the proposed broadband absorber. Subsequently, an array of periodically arranged graphene disks is positioned atop the upper layer, characterized by a disk radius a and a lattice period L. For this layer, the surface current density distribution over each graphene disk is derived and can be expressed as follows:

$$J_s(\rho) = \sigma_s\left[E_T^{ext}(\rho) + E_T^{\rho}(\rho)\right] \tag{7}$$

Here, $E_T^{ext}(\rho)$ denotes the externally applied transverse electric field, while $E_T^{\rho}(\rho)$ represents the transverse field induced by the charge accumulation on the graphene surface. The position vector of an arbitrary point on the graphene plane is defined as $\rho = x\hat{x} + y\hat{y}$.Under the quasi-static approximation, the field $E_T^{\rho}(\rho)$ can be expressed as the transverse gradient of the electrostatic potential generated by the surface charges on the graphene sheet, as given by:

$$E_T^{\rho}(\rho) = -\nabla_T\Phi_\rho(\rho) = -\nabla_T\int_S \frac{\rho_s(\rho')ds'}{4\pi\varepsilon_{eff}|\rho-\rho'|} \tag{8}$$

By employing the charge continuity equation, the following relation is derived:

$$\rho_s(\rho) = \frac{1}{j\omega}\nabla_T.J_s(\rho) \tag{9}$$

Hence, upon substituting Eq. (7) into Eq. (8) and subsequently inserting the resulting expression into Eq. (9), one arrives at the integral equation governing the surface current density within the quasi-static approximation, which can be written as:

$$\frac{J_s(\rho)}{\sigma_s} = E_T^{ext}(\rho) - \frac{1}{2j\omega\varepsilon_0}\nabla_T\int_S \frac{1}{2\pi|\rho-\rho'|}\nabla_T{}'.J_s(\rho')ds' \tag{10}$$

To solve this equation, we first consider the following eigenvalue problem defined on the disk.

$$\nabla_T\int_S \frac{1}{2\pi|\rho-\rho'|}\nabla_T{}'.\xi(\rho')ds' = -\lambda\xi(\rho),\ \ \xi(\rho).\hat{\rho}|_{\rho=a} = 0 \tag{11}$$

In this formulation, ξ represents the eigenfunction, and λ denotes the associated eigenvalue. It follows directly from the governing equation that ξ can be represented as the transverse gradient of a scalar potential, namely, $\xi = -\nabla_T\psi$ Consequently, the original vector eigenvalue problem is equivalently reduced to the following scalar eigenvalue problem:

$$\int_S \frac{1}{2\pi|\rho-\rho'|}\nabla_T{}'^2\psi(\rho')ds' = -\lambda\psi(\rho),\ \ \nabla_T\psi(\rho).\hat{\rho}|_{\rho=a} = 0 \tag{12}$$

Subsequently, by exploiting the cylindrical symmetry of the problem, the scalar function ψ is expanded in cylindrical coordinates as $\psi(\rho) = \psi_{mn}(\rho) = \exp(im\ \varphi)\ f_{mn}(\rho)$. Upon substituting this expression into Eq. (12), the following equation is obtained:

$$-\int_0^a g_m(\rho,\ \rho')\left[\frac{1}{\rho'}\frac{d}{d\rho'}\left(\rho'\frac{d\,f_{mn}}{d\rho'}\right) - m^2\frac{f_{mn}}{\rho'^2}\right]\rho'd\rho' = \lambda_{mn}\ f_{mn}(\rho) \tag{13}$$

where λ has been replaced by λ_{mn}, and

$$g_m(\rho,\ \rho') = \int_0^{2\pi}\frac{1}{2\pi|\rho-\rho'|}\exp[im\ (\varphi'-\varphi)]d\varphi' \tag{14}$$

Eq. (13) can be solved by expanding the functions $f_{mn}(\rho)$ in terms of Bessel functions. The eigenvalues and their corresponding eigenfunctions for $m = 1$ and $n = 1$ are summarized in Table 2.

The current distribution is expanded in terms of the eigenfunctions as follows:

$$J_s(\rho) = \sum_{m=-\infty}^{\infty}\sum_{n=1}^{\infty} A_{mn}\ \xi_{mn}(\rho) \tag{15}$$

Substituting this expansion into Eq. (10) and exploiting the orthogonality of the eigenfunctions, we obtain:

$$A_{mn} = \frac{2j\omega\varepsilon_0}{\beta_p(\omega) - \lambda_{mn}}\ \frac{\int_s E_T^{ext}(\rho).\ \xi_{mn}{}^*(\rho)\ ds}{\int_s|\ \xi_{mn}(\rho)|^2\ ds} \tag{16}$$

Therefore, to determine the resonance frequency of the graphene disk, it is sufficient to solve the equation $\beta_p(\omega) = \lambda_{mn}$. Accordingly, the proposed absorber operates based on this theoretical framework and exhibits broadband absorption over the frequency range from 0 to 2

Table 1
Eigenvalues and corresponding eigenfunctions for the first three modes.

Eigenfunction ($\boldsymbol{\psi_n}$)	Eigenvalue ($\mathbf{k_n}$)
$\psi_1 = w^{-\frac{1}{2}}\left[1.2\sin\left(\cos^{-1}\frac{2x}{w}\right) - 0.106\sin\left(3\cos^{-1}\frac{2x}{w}\right)\right]$	$0.737\ \pi/w$
$\psi_2 = w^{-\frac{1}{2}}\left[1.254\sin\left(2\cos^{-1}\frac{2x}{w}\right) - 0.302\sin\left(4\cos^{-1}\frac{2x}{w}\right)\right]$	$1.753\ \pi/w$
$\psi_3 = w^{-\frac{1}{2}}\left[0.308\sin\left(\cos^{-1}\frac{2x}{w}\right) + 1.19\sin\left(3\cos^{-1}\frac{2x}{w}\right) - 0.484\sin\left(5\cos^{-1}\frac{2x}{w}\right)\right]$	$2.748\ \pi/w$

Table 2
Eigenvalues and corresponding eigenfunctions for $m = 1$ and $n = 1,2,3$. In this table, J_1 denotes the first-order Bessel function of the first kind, and ξ_{1p} represents the p-th zero of the first-order Bessel function.

eigenfunction (f_{1n})	Eigenvalue (λ_{1n})
$f_{11} = \left[J_1\left(\frac{\xi_{11}\rho}{a}\right) - 0.06\ J_1\left(\frac{\xi_{12}\rho}{a}\right) + 0.22\ J_1\left(\frac{\xi_{13}\rho}{a}\right)\right]$	$\frac{1.1}{a}$
$f_{12} = \left[-0.25\ J_1\left(\frac{\xi_{11}\rho}{a}\right) - 0.965\ J_1\left(\frac{\xi_{12}\rho}{a}\right) + 0.085\ J_1\left(\frac{\xi_{13}\rho}{a}\right)\right]$	$\frac{4.92}{a}$
$f_{13} = \left[-0.12\ J_1\left(\frac{\xi_{11}\rho}{a}\right) + 0.162\ J_1\left(\frac{\xi_{12}\rho}{a}\right) + 0.97\ J_1\left(\frac{\xi_{13}\rho}{a}\right) - 0.1\ J_1\left(\frac{\xi_{14}\rho}{a}\right)\right]$	$\frac{8.12}{a}$

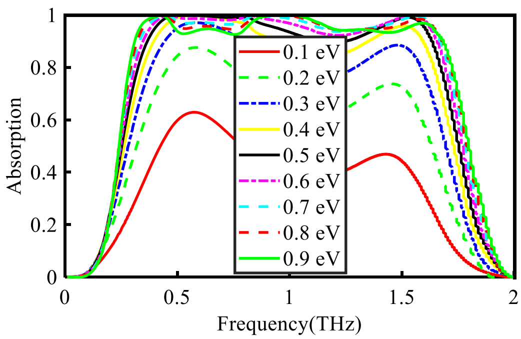

Fig. 2. The absorption spectrum of the proposed absorber for various chemical potentials.

THz. As illustrated in Fig. 1(c), both transverse electric (TE) and transverse magnetic TM polarizations are presented under normal incidence.

The proposed design is inherently scalable, such that the absorption bandwidth and absorption level can be effectively tuned by scaling the disk radius, the width of the graphene ribbons, and the periodicity of the graphene strips. In addition, the electromagnetic response of the structure can be dynamically controlled by adjusting the chemical potential of graphene. The sheet conductivity of monolayer graphene at optical frequencies is approximately equal to $\frac{e^2}{4\hbar}$. As the frequency decreases from the optical to lower ranges, the conductivity also diminishes correspondingly. Two fundamental parameters that characterize graphene's electrical behavior are: its universal optical conductivity $\frac{e^2}{4\hbar}$ at optical frequencies, and its exceptionally high carrier density and mobility in the DC regime, resulting in a conductivity nearly two orders of magnitude greater than that in the optical band. In the terahertz regime, graphene's surface conductivity depends sensitively on temperature, Fermi energy, carrier scattering rate, and operational frequency. When modeled as a conductive material, the real part of the intraband conductivity dominates its overall response. The general expressions are given by Eqs. (18) and (19):

$$\sigma(\omega) = \sigma^{intra} + \sigma^{inter} \tag{17}$$

$$Re\ \sigma^{inter}(\omega) = \frac{e^2}{4\hbar}\frac{\sinh\ (\omega/2k_BT)}{\cosh(E_F/2k_BT) + \ \cosh\ (\omega/2k_BT)} \tag{18}$$

$$Re\ \sigma^{intra}(\omega) = \frac{e^2}{4\hbar}\ \frac{8}{\pi}\ \frac{k_BT\tau/(2\pi\hbar)}{1+(\omega\tau)^2}\ln\left(2\cosh\left(\frac{E_F}{2k_B}\right)\right) \tag{19}$$

where T denotes the temperature, E_F is the Fermi energy, and τ represents the carrier relaxation time. Physically, the interband term corresponds to electron–hole pair generation and recombination, whereas the intraband component accounts for the response of free charge carriers. Under typical conditions, where the temperature is finite and $E_F \gg k_BT$, the real part of the intraband conductivity can be approximated as shown in Eq. (20) [85].

$$Re\ \sigma^{intra}(\omega) = \frac{e^2}{4\hbar}\ \frac{4}{\pi}\ \frac{E_F\tau/(2\pi\hbar)}{1+(\omega\tau)^2} \tag{20}$$

The electrical conductivity of graphene under externally applied electric and magnetic fields perpendicular to its plane can be expressed through the following tensor. In general, graphene exhibits anisotropic behavior.

$$\overline{\sigma} = \begin{bmatrix} \sigma_d & \sigma_h \\ -\sigma_h & \sigma_d \end{bmatrix} \tag{21}$$

The terms of σ_d and σ_h are derived using the well-known Kubo formalism [86].

$$\begin{aligned}\sigma_d = {} & \frac{e^2 v_f |eB_0|(\omega - j2\Gamma)}{-j\pi} \\ & \times \sum_{n=0}^{\infty}\left\{(f_d(M_n) - f_d(M_{n+1}) + f_d(-M_{n+1}) - f_d(M_n)) \times \left(1 - \frac{\Delta^2}{M_nM_{n+1}}\right)\right. \\ & \times \frac{1}{(M_{n+1}-M_n)^2 - (\omega - j2\Gamma)^2\hbar^2} + \left(1\right. \\ & \left.\left. + \frac{\Delta^2}{M_nM_{n+1}}\right)\frac{1}{(M_{n+1}-M_n)^2 - (\omega - j2\Gamma)^2\hbar^2}\right\}\end{aligned} \tag{22}$$

$$\begin{aligned}\sigma_h = {} & -\frac{e^2 {v_f}^2 eB_0}{\pi}\times \\ & \sum_{n=0}^{\infty}\left\{(f_d(M_n) - f_d(M_{n+1}) + f_d(-M_{n+1}) - f_d(M_n))\right. \\ & \times \left(1 - \frac{\Delta^2}{M_nM_{n+1}}\right) \times \frac{1}{(M_{n+1}-M_n)^2 - (\omega - j2\Gamma)^2\hbar^2} + \left(1\right. \\ & \left.\left. + \frac{\Delta^2}{M_nM_{n+1}}\right)\frac{1}{(M_{n+1}-M_n)^2 - (\omega - j2\Gamma)^2\hbar^2}\right\}\end{aligned} \tag{23}$$

In these expressions, $\hbar$ represents the reduced Planck constant, e is the electron charge, B_0 denotes the magnitude of the external magnetic flux density, Γ is the electron scattering rate, Δ stands for the excitonic gap, v_F refers to the Fermi velocity, and f_d and M_n are obtained from the relations given below [86].

$$f_d(\varepsilon) = \left(e^{(\varepsilon - u_c)/K_BT} + 1\right)^{-1} \tag{24}$$

$$M_n = \sqrt{\Delta^2 + 2n{v_f}^2|eB_0|\hbar} \tag{25}$$

For structures operating at room temperature or under weak external magnetic fields, the excitonic gap Δ can be assumed to approach zero. The subsequent relations are used to determine the chemical potential μ_c, and Fig. 2 illustrates the absorption spectra at different frequencies for varying chemical potential values.

$$\mu_C = \frac{\hbar}{e}v_f\sqrt{\frac{\pi\varepsilon_s V_g}{ed}} \tag{26}$$

In this relation, ε_s denotes the permittivity of the substrate, d represents the substrate thickness, and V_g is the applied gate voltage.

Numerical Simulation Setup: To evaluate the electromagnetic performance of the proposed structure, full-wave numerical simulations were performed using the time-domain solver of CST Studio Suite. To model the infinite periodic array of the absorber, Unit Cell boundary conditions were applied along the x- and y-axes. An Open (add space) boundary condition, functioning as a Perfectly Matched Layer (PML), was assigned along the z-axis to absorb outgoing waves. The structure was excited by a normally incident linearly polarized plane wave via a Floquet port.

To ensure the reproducibility and accuracy of the results, adaptive hexahedral meshing was employed. The global mesh density was set to at least 15 lines per wavelength at the maximum simulation frequency, with severe local mesh refinements applied at the dielectric interfaces and within the narrow gaps of the resonators to accurately capture localized field enhancements. Importantly, single-layer graphene was not modeled as a volumetric 3D structure, which would impose a severe computational burden due to its atomic thickness (~0.34 nm). Instead, it was simulated as a zero-thickness 2D surface (Surface Impedance boundary). The surface conductivity properties were defined by importing the frequency-dispersive complex conductivity (σ_s) derived analytically from the Kubo formula, allowing for precise and efficient modeling of graphene's plasmonic behavior.

An increase in the chemical potential of graphene leads to an

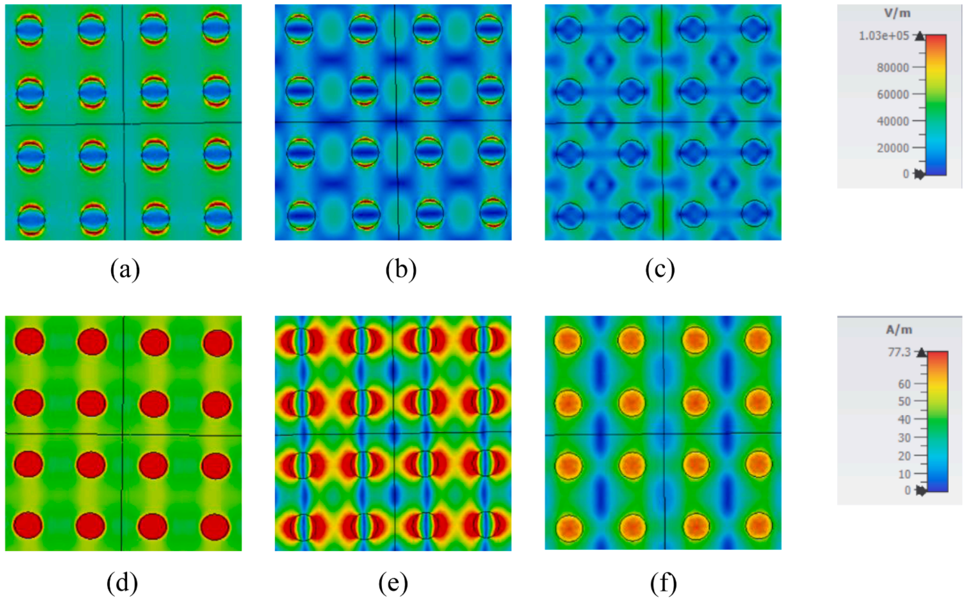

Fig. 3. The electric fields distributions at (a) 0.43 THz. (b) 0.94 THz. (c) 1.52 THz. (d) and the magnetic fields distributions at 0.43 THz. (e) 0.94 THz. (f) 1.52 THz.

enhancement in its electrical conductivity. According to the presented formulations, as the chemical potential and consequently the electrical conductivity of graphene increase, the transmission loss of the structure decreases. A higher chemical potential results in improved graphene conductivity, which in turn reduces ohmic losses and renders the graphene layer more conductive. As illustrated in Fig. 2, the optimal value of the chemical potential is found to be 0.6 eV. The electrical conductivity of graphene is frequency dependent and significant across three distinct frequency regimes:

$$1.\ \hbar\omega > 2E_F,\ \ 2.\ E_{12} < \hbar\omega < 2E_f,\ \ 3.\hbar w << 2E_F \tag{27}$$

To model graphene as an extremely thin plasmonic layer, its operating regime must correspond to region 3. In this specific frequency range, the conductivity exhibits a real part that is small and a positive imaginary part. Consequently, within this regime, graphene presents an equivalent permittivity characterized by a negative real component and a small imaginary component. This behavior confirms that graphene effectively mimics an ultrathin plasmonic layer. Under these stipulated conditions, the propagation constant for the surface plasmon wave satisfies $\sigma_{inter} \approx 0$, and the relationship is given by [87]:

$$\sigma_s \cong \sigma_{intra} \cong \frac{e^2 E_F}{\pi\hbar^2}\ \frac{i}{\omega + i\tau^{-1}} \tag{28}$$

Therefore, under the mentioned circumstances, graphene is equivalent to an extremely thin plasmonic layer.

In fact, one of the most significant advantages of graphene-based circuits is the tunability of the operating frequency band through the application of a gate voltage. Moreover, graphene enables bias-controlled manipulation of radiative characteristics. It has been shown that at low frequencies, the intraband contribution of graphene surface conductivity dominates the overall response, whereas at higher frequencies, the interband contribution becomes predominant. The strong field confinement of surface plasmon polaritons (SPPs) supported by graphene is particularly advantageous for the realization of graphene-based plasmonic circuits operating in the terahertz frequency range. As observed in Fig. 3, SPP propagation along graphene leads to pronounced wave localization and can be effectively tuned by external electric or magnetic fields.

The primary goal of the proposed absorber is to realize unity absorption ($A = 1$). This condition can only be attained by simultaneously suppressing reflection and transmission. Reflection can be effectively eliminated through perfect impedance matching between the absorber and free space. Furthermore, negligible transmission is ensured by selecting a gold back layer whose thickness is much larger than the skin depth of gold. To avoid the computational cost associated with full-wave numerical simulations, the equivalent circuit model illustrated in Fig. 4 (a) is employed. In this approach, graphene is represented by lumped circuit components, including resistive, inductive, and capacitive elements, enabling an analytical evaluation of the overall impedance of the structure. The governing relations of the transmission-line representation and the corresponding definitions of the circuit elements are given below [82]:

$$R_1 = \frac{D}{s_1^2}\frac{\pi\hbar^2}{e^2 E_F \tau} \tag{29}$$

$$L_1 = \frac{D}{s_1^2}\frac{\pi\hbar^2}{e^2 E_F} \tag{30}$$

$$C_1 = \frac{s_1^2}{D}\frac{2\varepsilon_{eff1}}{q_1} \tag{31}$$

$$s_1^2 \cong \frac{s_1^2}{D}W \tag{32}$$

Here, D and W denote the periodicity and the width of the graphene ribbons, respectively. The parameter $\varepsilon_{eff1} = \varepsilon_0 n_s^2$ represents the effective permittivity of the media adjacent to the graphene ribbons, while q_1 corresponds to the fundamental eigenvalue associated with the current distribution on the ribbons. The values of q_1 for various ratios of $\frac{W}{D}$ are listed in Table 3.

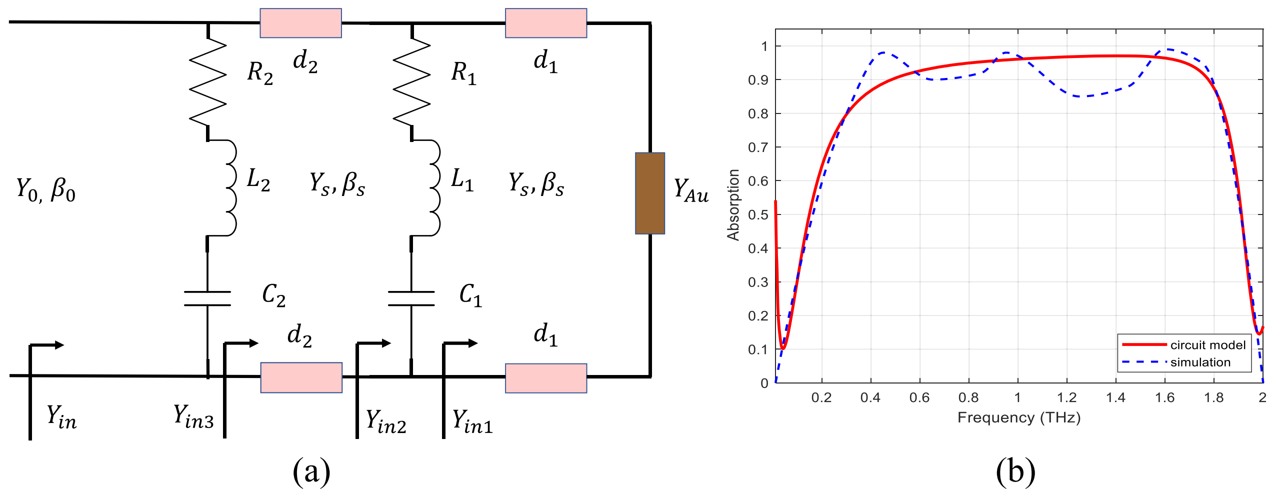

Fig. 4. (a). The transmission line model of proposed absorber (b). Comparison between the transmission line model and simulation results.

$$R_2 = \frac{\hbar^2}{e^2 E_F \tau} \frac{K_1 L^2}{\pi s_2^2} \tag{33}$$

$$L_2 = \frac{\hbar^2}{e^2 E_F} \frac{K_1 L^2}{\pi s_2^2} \tag{34}$$

$$C_2 = \frac{\varepsilon_{eff2}}{q_{11}} \frac{\pi^2 s_2^2}{K_1 L^2} \tag{35}$$

Here q_{11} is the first eigenvalue of the equation governing the current on the disks. Values of q_{11} for different $2a/L$ have been given in Table 4., [88], $s_2 = 0.6087a$, $K_1 = 1.2937$.

$$Y_{in1} = -j.Y_s.\cot(\beta_s.d_1) \tag{36}$$

$$Z_{G1} = R_1 + j\omega L_1 + \frac{1}{j\omega C_1} = \frac{D\pi\hbar^2}{s_1^2 e^2 E_F \tau} + j\omega\left(\frac{D\pi\hbar^2}{s_1^2 e^2 E_F}\right) + \frac{1}{j\omega} \frac{Dq_1}{2s_1^2\ \varepsilon_{eff1}} \tag{37}$$

$$Y_{G1} = 1\Big/\left(\frac{D\pi\hbar^2}{s_1^2 e^2 E_F \tau} + j\omega\left(\frac{D\pi\hbar^2}{s_1^2 e^2 E_F}\right) + \frac{1}{j\omega} \frac{Dq_1}{2s_1^2\ \varepsilon_{eff1}}\right) \tag{38}$$

$$Z_{G2} = R_2 + j\omega L_2 + \frac{1}{j\omega C_2} = \frac{\hbar^2 K_1 L^2}{e^2 E_F \tau\ \pi s_2^2} + j\omega\left(\frac{\hbar^2 K_1 L^2}{e^2 E_F \pi s_2^2}\right) + \frac{1}{j\omega} \frac{q_{11}}{\varepsilon_{eff2}} \frac{K_1 L^2}{\pi^2 s_2^2} \tag{39}$$

$$Y_{G2} = 1\Big/\left(\frac{\hbar^2 K_1 L^2}{e^2 E_F \tau\ \pi s_2^2} + j\omega\left(\frac{\hbar^2 K_1 L^2}{e^2 E_F \pi s_2^2}\right) + \frac{1}{j\omega} \frac{q_{11}}{\varepsilon_{eff2}} \frac{K_1 L^2}{\pi^2 s_2^2}\right) \tag{40}$$

$$\begin{aligned} Y_{in2} &= Y_{in1} + Y_{G1} \\ &= -j.Y_s.\cot(\beta_s.d_1) + 1\Big/\left(\frac{D\pi\hbar^2}{s_1^2 e^2 E_F \tau} + j\omega\left(\frac{D\pi\hbar^2}{s_1^2 e^2 E_F}\right) + \frac{1}{j\omega} \frac{Dq_1}{2s_1^2\ \varepsilon_{eff1}}\right) \end{aligned} \tag{41}$$

$$\begin{aligned} Y_{in3} &= Y_s.\frac{Y_{in2} + jY_s.\tan(\beta_s.d_2)}{Y_s + jY_{in2}.\tan(\beta_s.d_2)} \\ &= Y_s.\frac{-j.Y_s.\cot(\beta_s.d_1) + \dfrac{1}{\frac{D\pi\hbar^2}{s_1^2 e^2 E_F \tau} + j\omega\left(\frac{D\pi\hbar^2}{s_1^2 e^2 E_F}\right) + \frac{1}{j\omega}\frac{Dq_1}{2s_1^2\ \varepsilon_{eff1}}} + jY_s.\tan(\beta_s.d_2)}{Y_s + j\left[-j.Y_s.\cot(\beta_s.d_1) + \dfrac{1}{\frac{D\pi\hbar^2}{s_1^2 e^2 E_F \tau} + j\omega\left(\frac{D\pi\hbar^2}{s_1^2 e^2 E_F}\right) + \frac{1}{j\omega}\frac{Dq_1}{2s_1^2\ \varepsilon_{eff1}}}.\tan(\beta_s.d_2)\right]} \end{aligned} \tag{42}$$

$$\begin{aligned} Y_{in} &= Y_{in3} + Y_{G2} \\ &= Y_s.\frac{-j.Y_s.\cot(\beta_s.d_1) + \dfrac{1}{\frac{D\pi\hbar^2}{s_1^2 e^2 E_F \tau} + j\omega\left(\frac{D\pi\hbar^2}{s_1^2 e^2 E_F}\right) + \frac{1}{j\omega}\frac{Dq_1}{2s_1^2\ \varepsilon_{eff1}}} + jY_s.\tan(\beta_s.d_2)}{Y_s + j\left[-j.Y_s.\cot(\beta_s.d_1) + \dfrac{1}{\frac{D\pi\hbar^2}{s_1^2 e^2 E_F \tau} + j\omega\left(\frac{D\pi\hbar^2}{s_1^2 e^2 E_F}\right) + \frac{1}{j\omega}\frac{Dq_1}{2s_1^2\ \varepsilon_{eff1}}}.\tan(\beta_s.d_2)\right]} \\ &\quad + 1\Big/\left(\frac{\hbar^2 K_1 L^2}{e^2 E_F \tau\ \pi s_2^2} + j\omega\left(\frac{\hbar^2 K_1 L^2}{e^2 E_F \pi s_2^2}\right) + \frac{1}{j\omega} \frac{q_{11}}{\varepsilon_{eff2}} \frac{K_1 L^2}{\pi^2 s_2^2}\right) \end{aligned} \tag{43}$$

Table 3
Eigenvalue q_1 for different fill factors.

W/D	0.1	0.2	0.3	0.4	0.5	0.6	0.7	0.8	0.9
$q_1 W/\pi$	0.734	0.725	0.710	0.689	0.658	0.620	0.571	0.507	0.420

Table 4
The eigenvalues of graphene disk array.

$2a/L$	0.1	0.2	0.3	0.4	0.5	0.6	0.7	0.8	0.9
$q_{11}\ a$	0.539	0.536	0.533	0.530	0.527	0.499	0.472	0.444	0.417

$$\Gamma = \frac{Y_0 - Y_{in}}{Y_0 + Y_{in}} = \frac{Y_0 - Y_{in}}{Y_0 + Y_{in}} = \frac{Y_0 - Y_s.\dfrac{-j.Y_s.\cot(\beta_s.d_1) + \dfrac{1}{\dfrac{D\pi\hbar^2}{s_1^2 e^2 E_F \tau} + j\omega\left(\dfrac{D\pi\hbar^2}{s_1^2 e^2 E_F}\right) + \dfrac{1}{j\omega}\dfrac{Dq_1}{2s_1^2\ \varepsilon_{eff1}}} + jY_s.\tan(\beta_s.d_2)}{Y_s + j\left[-j.Y_s.\cot(\beta_s.d_1) + \dfrac{1}{\dfrac{D\pi\hbar^2}{s_1^2 e^2 E_F \tau} + j\omega\left(\dfrac{D\pi\hbar^2}{s_1^2 e^2 E_F}\right) + \dfrac{1}{j\omega}\dfrac{Dq_1}{2s_1^2\ \varepsilon_{eff1}}}.\tan(\beta_s.d_2)\right]} + 1\Big/\left(\dfrac{\hbar^2 K_1 L^2}{e^2 E_F \tau\ \pi s_2^2} + j\omega\left(\dfrac{\hbar^2 K_1 L^2}{e^2 E_F \pi s_2^2}\right) + \dfrac{1}{j\omega}\dfrac{q_{11}}{\varepsilon_{eff2}}\dfrac{K_1 L^2}{\pi^2 s_2^2}\right)}{Y_0 + Y_s.\dfrac{-j.Y_s.\cot(\beta_s.d_1) + \dfrac{1}{\dfrac{D\pi\hbar^2}{s_1^2 e^2 E_F \tau} + j\omega\left(\dfrac{D\pi\hbar^2}{s_1^2 e^2 E_F}\right) + \dfrac{1}{j\omega}\dfrac{Dq_1}{2s_1^2\ \varepsilon_{eff1}}} + jY_s.\tan(\beta_s.d_2)}{Y_s + j\left[-j.Y_s.\cot(\beta_s.d_1) + \dfrac{1}{\dfrac{D\pi\hbar^2}{s_1^2 e^2 E_F \tau} + j\omega\left(\dfrac{D\pi\hbar^2}{s_1^2 e^2 E_F}\right) + \dfrac{1}{j\omega}\dfrac{Dq_1}{2s_1^2\ \varepsilon_{eff1}}}.\tan(\beta_s.d_2)\right]} + 1\Big/\left(\dfrac{\hbar^2 K_1 L^2}{e^2 E_F \tau\ \pi s_2^2} + j\omega\left(\dfrac{\hbar^2 K_1 L^2}{e^2 E_F \pi s_2^2}\right) + \dfrac{1}{j\omega}\dfrac{q_{11}}{\varepsilon_{eff2}}\dfrac{K_1 L^2}{\pi^2 s_2^2}\right)} \tag{44}$$

$$A = 1 - \left| \frac{Y_0 - Y_s.\dfrac{-j.Y_s.\cot(\beta_s.d_1) + \dfrac{1}{\dfrac{D\pi\hbar^2}{s_1^2 e^2 E_F \tau} + j\omega\left(\dfrac{D\pi\hbar^2}{s_1^2 e^2 E_F}\right) + \dfrac{1}{j\omega}\dfrac{Dq_1}{2s_1^2\ \varepsilon_{eff1}}} + jY_s.\tan(\beta_s.d_2)}{Y_s + j\left[-j.Y_s.\cot(\beta_s.d_1) + \dfrac{1}{\dfrac{D\pi\hbar^2}{s_1^2 e^2 E_F \tau} + j\omega\left(\dfrac{D\pi\hbar^2}{s_1^2 e^2 E_F}\right) + \dfrac{1}{j\omega}\dfrac{Dq_1}{2s_1^2\ \varepsilon_{eff1}}}.\tan(\beta_s.d_2)\right]} + \dfrac{1}{\dfrac{\hbar^2 K_1 L^2}{e^2 E_F \tau\ \pi s_2^2} + j\omega\left(\dfrac{\hbar^2 K_1 L^2}{e^2 E_F \pi s_2^2}\right) + \dfrac{1}{j\omega}\dfrac{q_{11}}{\varepsilon_{eff2}}\dfrac{K_1 L^2}{\pi^2 s_2^2}}}{Y_0 + Y_s.\dfrac{-j.Y_s.\cot(\beta_s.d_1) + \dfrac{1}{\dfrac{D\pi\hbar^2}{s_1^2 e^2 E_F \tau} + j\omega\left(\dfrac{D\pi\hbar^2}{s_1^2 e^2 E_F}\right) + \dfrac{1}{j\omega}\dfrac{Dq_1}{2s_1^2\ \varepsilon_{eff1}}} + jY_s.\tan(\beta_s.d_2)}{Y_s + j\left[-j.Y_s.\cot(\beta_s.d_1) + \dfrac{1}{\dfrac{D\pi\hbar^2}{s_1^2 e^2 E_F \tau} + j\omega\left(\dfrac{D\pi\hbar^2}{s_1^2 e^2 E_F}\right) + \dfrac{1}{j\omega}\dfrac{Dq_1}{2s_1^2\ \varepsilon_{eff1}}}.\tan(\beta_s.d_2)\right]} + 1/\left(\dfrac{\hbar^2 K_1 L^2}{e^2 E_F \tau\ \pi s_2^2} + j\omega\right.} \right| \tag{45}$$

In this study, a cost function is employed to optimize six parameters, namely R_1, L_1, C_1, R_2, L_2, and C_2. The objective of this cost function is to determine the optimal values of the resistive, inductive, and capacitive elements associated with both the graphene ribbon layer and the graphene disk layer, such that maximum absorption and a wide operational bandwidth are achieved at the resonance frequencies as well as over the desired frequency range.

Mathematically, this cost function (CF) is defined as the Sum of Squared Errors (SSE) between the absorption response of the full-wave simulation and that of the equivalent circuit model, which can be explicitly expressed as:

$$CF = SSE = \sum_{i=1}^{N} \left[A_{simulation}(f_i) - A_{circuit}(f_i)\right]^2$$

where N is the total number of frequency points, $A_{simulation}(f_i)$ represents the simulated absorption magnitude, and $A_{circuit}(f_i)$ is the absorption calculated from the equivalent circuit model at the i th frequency point (f_i). By minimizing this cost function, the optimal values of these six parameters are determined and summarized in Table 5, along with the corresponding SSE value. As demonstrated in Fig. 4(b), an excellent agreement is observed between the proposed analytical model and the full-wave simulation results.

Table 5
The values of optimized parameters.

Parameters	R_1	L_1	C_1	R_2	L_2	C_2	SSE
Values	10.46 Ω	17.2 nH	0.09 fF	257.94 Ω	93.6 pH	0.06 fF	1.573

It is noteworthy that the extracted capacitance values are highly minimized (e.g., 0.09 fF and 0.06 fF). These sub-femtofarad (attofarad range) values are physically plausible and expected for the proposed structure. At the nanoscale, the effective cross-sectional areas of the gaps and interacting metallic/graphene patches are extremely small, which directly leads to such diminutive gap and fringing capacitances, consistent with standard THz metamaterial circuit models.

To elucidate the physical mechanism behind the achieved broadband absorption, the effective electromagnetic parameters of the proposed structure are extracted using the standard parameter retrieval method based on the simulated S-parameters (S_{11} and S_{21}). Fig. 5 illustrates the extracted normalized equivalent impedance (Z), effective permittivity (ε_{eff}), and effective magnetic permeability (μ_{eff}).

As shown in Fig. 5(c), across the primary absorption bands, the real part of the normalized impedance (Re(Z)) is maintained close to 1, while the imaginary part (Im(Z)) oscillates near 0. This condition confirms excellent broadband impedance matching between the proposed absorber and free space, which drastically minimizes the reflection coefficient at the incident interface. Furthermore, Fig. 5.(a) and Fig. 5.(b) depict the effective magnetic permeability and dielectric constant, respectively. The strong variations and multiple resonant peaks in ε_{eff} and μ_{eff} demonstrate the simultaneous excitation of continuous electric and magnetic resonances within the metamaterial structure. Specifically, the highly negative real part of the permittivity at lower frequencies verifies the strong plasmonic response of the utilized graphene layer [89]. The synergistic combination of these localized electric and magnetic responses allows for manipulating the effective macroscopic parameters to achieve $Z \approx 1$, ultimately leading to the proposed

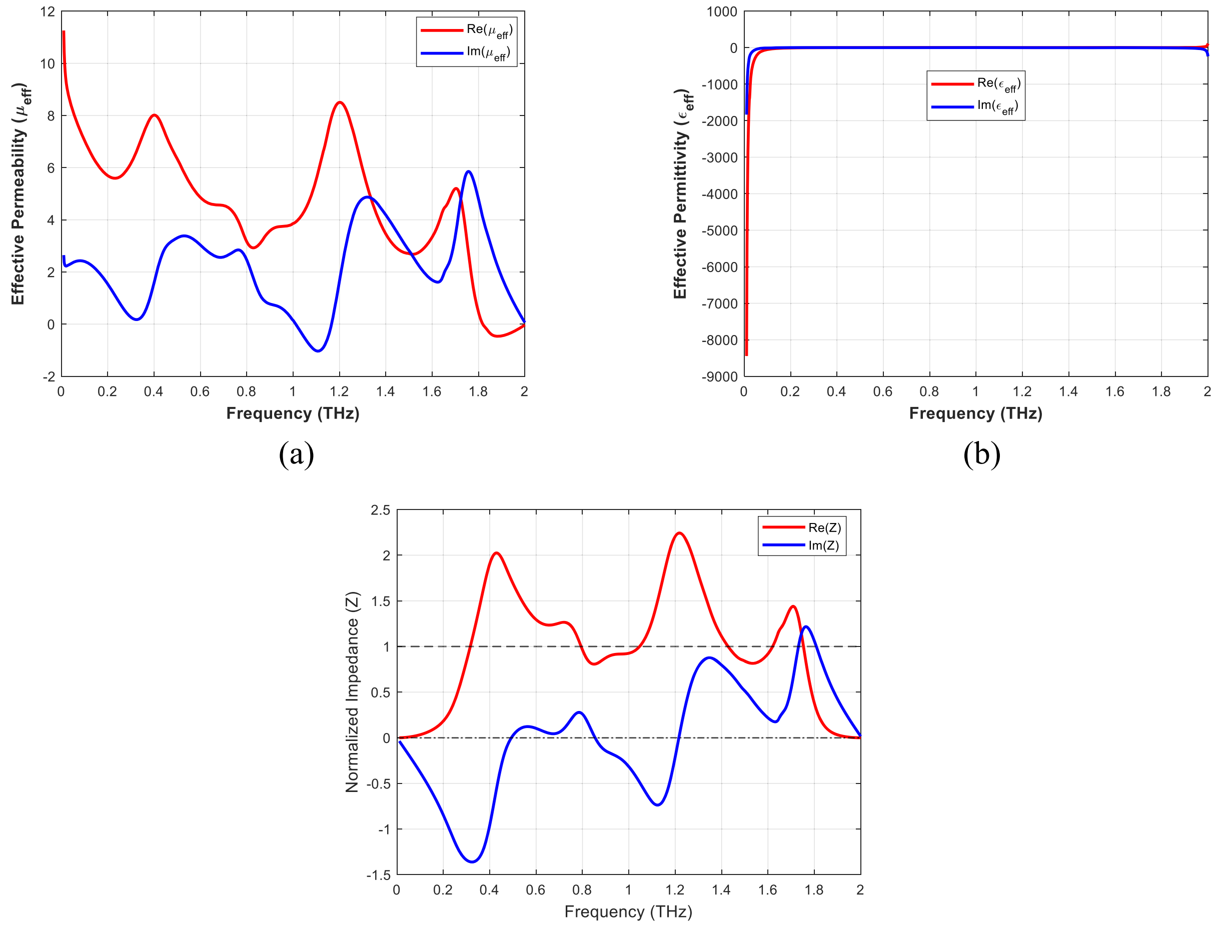

Fig. 5. Extracted effective electromagnetic parameters of the proposed structure versus frequency: (a) real and imaginary parts of effective permeability (μ_{eff}). (b). real and imaginary parts of effective permittivity (ε_{eff}). (c). real and imaginary parts of normalized impedance (Z).

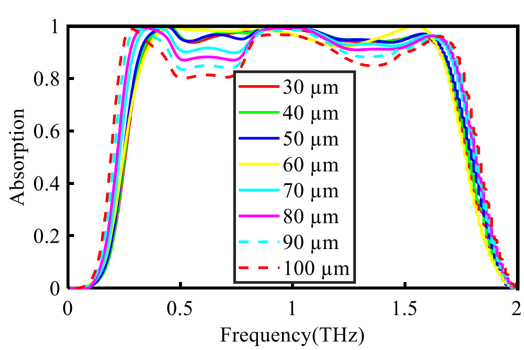

Fig. 6. The absorption spectra of the proposed absorber were analyzed for various radius of graphene disks for second layer (a).

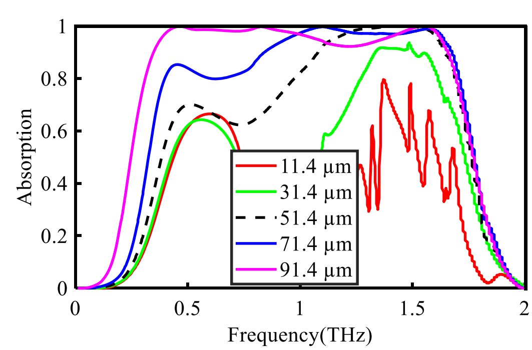

Fig. 7. The absorption spectra of the proposed absorber were analyzed for various width of graphene ribbon for first layer (w).

broadband absorption.

One of the most critical tasks accompanying the structural design is the investigation of the absorber's electromagnetic behavior and its sensitivity to variations in the key design parameters. Accordingly, the effects of these parameters are systematically examined in the following section.

As shown in Fig. 6, the radii of the graphene disk array are systematically varied, and full-wave simulations are performed for each updated configuration. In this structure, the disk radius is selected to simultaneously maximize the absorption bandwidth and the absorption magnitude. Based on this parametric analysis, the optimal radius of the graphene disks is determined to be 60 µm. At this value, nearly perfect absorption is achieved over a broad frequency range.

In this section, the effect of reducing the width of the graphene ribbons is investigated. The ribbon width is one of the key parameters influencing the absorption performance of the proposed structure. As the width of the graphene ribbons decreases, the characteristic impedance of the absorber increases. Consequently, a higher level of current-related losses is expected for narrower ribbons. To examine this effect, the ribbon width is gradually reduced from 91.4 µm to 11.4 µm, and the

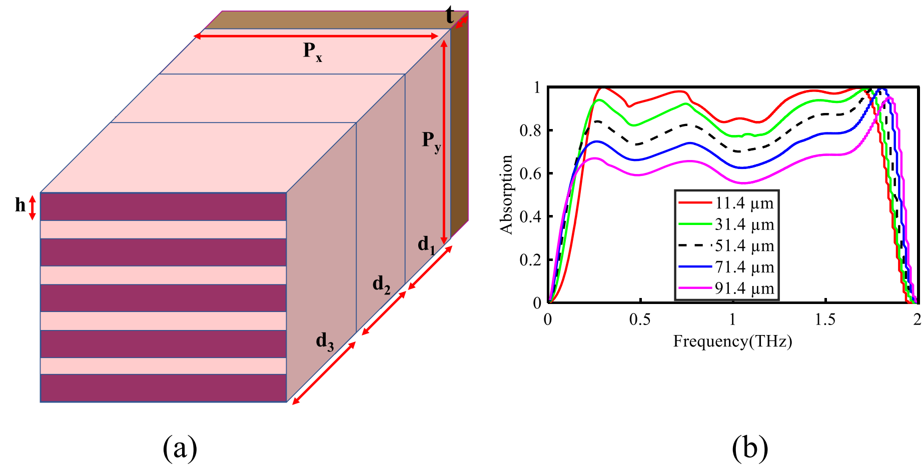

Fig. 8. (a). The unit cell of the proposed 3-layer absorber with horizontal ribbons. (b). The absorption spectra of the proposed structure were analyzed for various width of graphene ribbon for third layer (w).

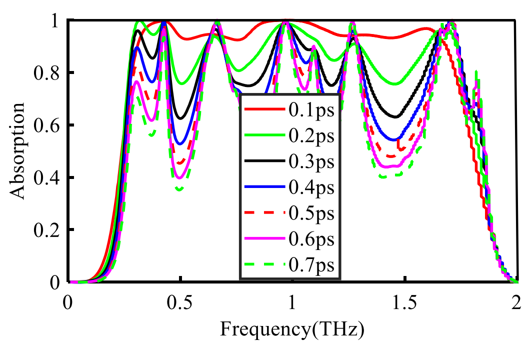

Fig. 9. The absorption spectra of the proposed absorber for the various relaxation time values.

absorber is redesigned and simulated for each case. The corresponding simulation results are presented in Fig. 7. The plots clearly illustrate the influence of the graphene ribbon width on the absorption characteristics. As observed, decreasing the ribbon width leads to increased losses within the structure. Based on this analysis, the optimal performance is achieved for a ribbon width of 91.4 μm in the first graphene layer, with a periodicity D of 118 μm.

At this stage, an additional layer is incorporated into the proposed absorber. This layer consists of a SiO_2 dielectric spacer with a thickness of $d_3 = 50\ um$, followed by a periodic array of graphene ribbons oriented orthogonally to the graphene ribbons in the first layer, as illustrated in Fig. 8(a). The graphene ribbons in this layer are assumed to be infinitely long along the x-direction. Due to their horizontal orientation, the optimal ribbon width in this configuration, unlike the previous case, corresponds to the minimum achievable width. Simulation results indicate that, in this configuration, increasing the ribbon width leads to enhanced current-related losses. Similar to the previous analysis, the absorber is redesigned and simulated for each considered ribbon width, and the resulting absorption spectra are presented in Fig. 8(b). Based on these results, the optimal ribbon width for this layer is found to be 11.4 μm.

The relaxation time of sheet graphene at low temperatures, as reported from DC measurements, typically ranges from 10 to 500 fs. As illustrated in Fig. 9, the relaxation time is varied from 0.1 to 0.7 ps, and the corresponding simulation results are presented. It is observed that the optimal absorption performance is achieved for a relaxation time of 0.1 ps. As the relaxation time increases beyond this value, the absorption response gradually departs from a broadband profile and evolves into a multi-resonant behavior.

The absorber's sensitivity to polarization is examined. Fig. 10 shows that the absorber responds equally to TE (Transverse Electric) and TM (Transverse Magnetic) polarization. In the case of TE polarization, the electric field vector lies in the plane of incidence, meaning that it is perpendicular to the direction of propagation and to the magnetic field vector. Conversely, for TM polarization, the magnetic field vector is aligned in the plane of incidence, while the electric field vector is perpendicular to both the direction of propagation and the magnetic

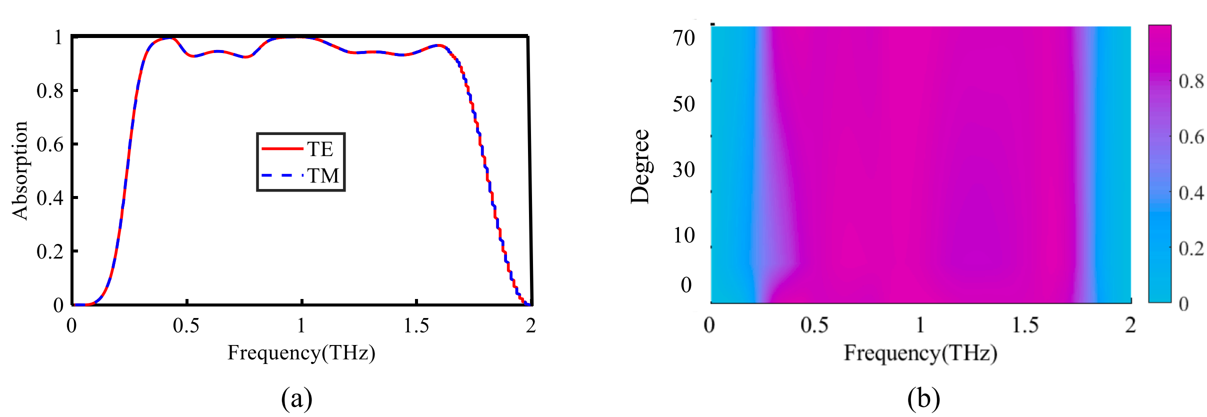

Fig. 10. (a). The absorption spectra for TE and TM modes for normal incidence (b). TE and TM polarization for different angles.

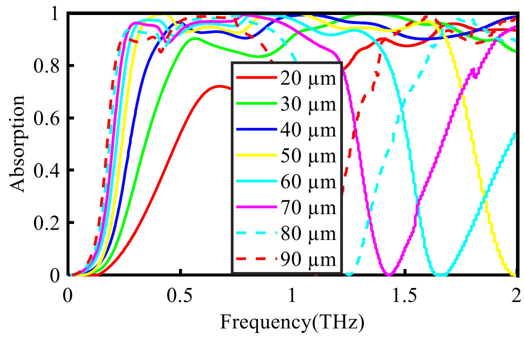

Fig. 11. The absorption spectra for different thicknesses for both dielectric layers ($d_1 = d_2$).

field vector.

The proposed absorber exhibits polarization-insensitive behavior, as the absorption spectra for both transverse electric (TE) and transverse magnetic (TM) polarizations are identical. In addition, as shown in Fig. 9 (b), the absorber is simulated for oblique incidence angles ranging from 0° to 70° The results demonstrate that the absorption response of the designed structure remains stable with respect to variations in the angle of incidence and is identical for both TE and TM polarizations.

The thickness of the dielectric substrate must be much smaller than the surface plasmon wavelength. Increasing the substrate thickness up to a certain limit leads to a reduction in losses. Accordingly, based on the simulation results presented in Fig. 11, the optimal thickness for both dielectric layers is determined to be 50 μm. Employing this thickness for the dielectric substrates results in improved impedance matching and achieves an optimal absorption bandwidth.

Based on the comprehensive parametric studies conducted in the preceding sections, the optimal dimensions for the proposed absorber have been finalized to achieve the maximum absorption and broadest bandwidth. For the convenience of the reader and to provide a clear overview of the structural design, the final optimized values for all key geometric parameters are summarized in Table 6.

Although this study primarily focuses on numerical calculations, the proposed optimized structure is practically feasible and can be fabricated using standard nanofabrication techniques. First, the bottom metallic ground plane can be deposited on a substrate using electron beam evaporation or magnetron sputtering. Next, the dielectric spacer layer can be formed via plasma-enhanced chemical vapor deposition (PECVD) or spin-coating, depending on the chosen material. For the graphene layer, high-quality single-layer graphene can be grown on a copper foil via Chemical Vapor Deposition (CVD) and then transferred onto the dielectric layer using a standard wet-transfer method. Finally, the top patterned structure can be precisely defined using Electron Beam Lithography (EBL) or standard photolithography, followed by Reactive Ion Etching (RIE) or a lift-off process to achieve the designed unit cell geometry. Furthermore, the chemical potential of the graphene layer can be practically controlled by fabricating gating pads and applying an external bias voltage.

4. Smith chart analysis

Based on the points marked in the Smith chart as shown in Fig. 12, two important impedance points can be identified, namely $Z_1 = (0.132 + j13.8)\Omega$ and $Z_2 = (0.0196 - j5.99)\Omega$, which correspond to the two main absorption resonances of the proposed structure. As can be observed from the Smith chart, the red trajectory approaches the center of the chart and crosses the real axis multiple times, indicating impedance matching at more than one frequency. This behavior is a clear signature of broadband impedance matching. Consequently, the structure approaches the impedance matching condition at several distinct frequencies. Each point that is closer to the center of the Smith chart corresponds to a smaller reflection coefficient magnitude $|\Gamma|$ and, therefore, a higher absorption level. In the vicinity of both resonances, the trajectory moves closer to the center, demonstrating that the observed absorption peaks are fully consistent with the Smith chart analysis. At the first resonance, the imaginary part of the impedance exhibits a large positive value, indicating a predominantly inductive behavior. The physical origin of this resonance is associated with loop currents and strong magnetic field coupling, and the absorption mechanism can be classified as a structural resonance. In contrast, the second resonance is characterized by a negative imaginary part of the impedance, revealing a dominant capacitive behavior. The physical origin of this resonance arises from graphene surface plasmons and carrier density oscillations, and the absorption mechanism is therefore plasmonic in nature. As a result, two distinct resonances with different physical mechanisms are observed. The overlap of these resonances leads to the formation of broadband absorption. From the Smith chart, it can be concluded that the proposed absorber operates as a broadband absorber rather than a single-frequency one, since the impedance trajectory is continuous and spiral-like, traverses different resistance and reactance regions, and approaches the chart center more than once. Furthermore, as evident from the figure, the absorber exhibits stable impedance matching, as the trajectory shows no abrupt jumps and the impedance varies continuously with frequency. This behavior indicates stable impedance matching and low sensitivity to frequency variations, which is a critically important feature for practical terahertz (THz) applications.

The physical mechanism driving the near-perfect, ultra-broadband absorption of the proposed structure is fundamentally rooted in the concept of macroscopic impedance matching combined with overlapping multiple resonances. By carefully optimizing the geometric pa-

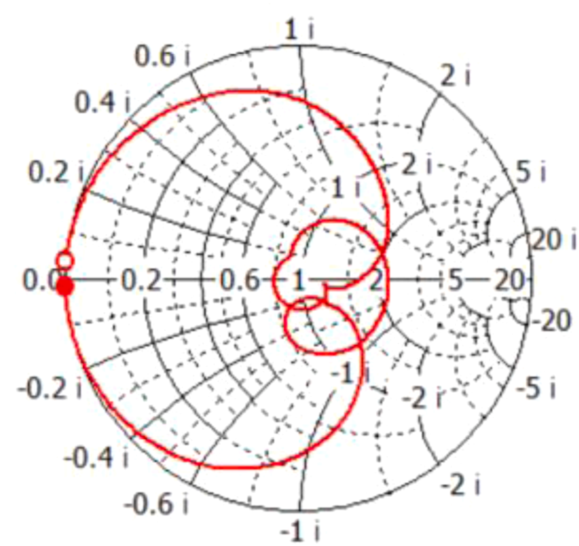

Fig. 12. The smith chart of the proposed absorber.

Table 6
Summary of the final optimized geometric parameters of the proposed structure.

Parameters	$a(\mu m)$	$L(\mu m)$	$w(\mu m)$	$D(\mu m)$	$d_1(\mu m)$	$d_2(\mu m)$	$t(\mu m)$	τ(ps)	$P_x = P_y(\mu m)$
Optimized Values	60	218.7	91.4	118	50	50	10	0.1	563.4

rameters of the unit cell and the thickness of the dielectric spacer, the effective input impedance of the metamaterial absorber is accurately matched to the free-space impedance ($Z_{in} \approx Z_0$). This impedance matching minimizes the reflection of incident waves at the air-absorber interface. Simultaneously, the continuous metallic ground plane blocks any transmission ($T = 0$), forcing the incident electromagnetic energy to be trapped within the structure. The ultra-broadband nature of the absorption spectrum is realized through the superposition of multiple adjacent resonant modes generated by the distinct geometric features of the top patterned layer. When these individual resonances are excited simultaneously, they merge into a single, continuous, and highly efficient broad absorption band spanning the THz regime.

At a microscopic level, the strong electromagnetic wave dissipation is primarily governed by the excitation of localized surface plasmon resonances (LSPR) on the patterned graphene layer. When the incident THz wave interacts with the structure, it induces strong electric field confinements, highly concentrated at the edges and gaps of the graphene resonators. This localized field enhancement effectively traps the incident electromagnetic energy. Coupled with the magnetic resonance formed within the intermediate dielectric substrate between the top graphene layer and the bottom ground plane the trapped energy is efficiently dissipated into heat through the inherent Ohmic losses of the graphene layer. Thus, the synergistic effect of both electric and magnetic resonances ensures maximum energy confinement and subsequent absorption.

Furthermore, a critical advantage of the proposed design is its dynamic tunability, which relies on the unique optoelectronic properties of graphene. According to the Kubo formula, the surface conductivity of graphene in the THz frequency range is highly dependent on its Fermi energy (E_f). By applying an external bias voltage or via chemical doping, the Fermi energy can be actively manipulated, thereby directly altering the surface carrier density. Modifying the Fermi energy changes the equivalent impedance of the graphene resonators, which consequently shifts the plasmonic resonance frequencies and modulates the absorption amplitude. This dynamic physical mechanism enables real-time tuning of the absorber's operational bandwidth and intensity without the need to physically alter the geometrical dimensions of the structure, validating its high potential for active THz devices.

One of the key advantages of broadband absorbers in sensing applications is their wide spectral coverage and capability for the simultaneous detection of multiple analytes. Many chemical, biological, and pharmaceutical substances exhibit absorption at several distinct frequencies in the terahertz regime due to the presence of multiple vibrational modes. A broadband absorber can interact concurrently with all of these absorption features in an unknown sample, thereby producing an integrated response. This characteristic significantly facilitates initial screening and qualitative identification processes. In practical sensing scenarios, samples are often composed of multiple constituents, such as drug mixtures or combinations of different proteins. When a broadband absorber is engineered to maintain sensitivity over a wide frequency range, it can effectively capture the cumulative influence of the simultaneous presence of multiple substances within that spectral band. In such cases, the sensing mechanism relies on the overall spectral response rather than the detection of a single narrow resonance peak. Moreover, if the terahertz source employed in the sensing system experiences slight frequency fluctuations or minor optical misalignment, narrowband absorbers may rapidly lose their effectiveness. In contrast, due to their extended absorption bandwidth, broadband absorbers exhibit significantly enhanced robustness and operational stability against small variations in source frequency and alignment errors. In this section, the refractive index sensing capability of the proposed absorber is investigated by assuming that the analyte layer is deposited directly onto the structure. The corresponding absorption spectra for various refractive index values are presented in Fig. 13. The refractive index is varied from 1.00 to 1.09 with a step size of 0.01. The results clearly demonstrate a systematic shift of the absorption response toward lower frequencies as the refractive index increases, confirming the suitability of the absorber for refractive index sensing applications. The sensitivity of the proposed sensor is evaluated by calculating the slope of the resonance frequency shift as a function of the refractive index, yielding a sensitivity of 3.3 THz/RIU

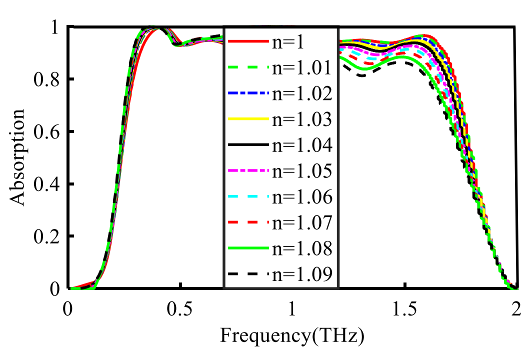

Fig. 13. The absorption spectrum for different analyte refractive indices.

To evaluate the sensing performance, it should be noted that in broadband absorbers, unlike typical narrowband sensors, the sensitivity is generally calculated by tracking the frequency shift of the absorption band edges or specific local resonance peaks. The sensitivity (S) is defined as $s = \Delta f / \Delta n$, where Δf is the resonance frequency shift and Δn is the change in the background refractive index. As depicted in Fig. 13, while the overall broad absorption band remains stable, the higher-frequency edge of the absorption band (specifically the local resonance peak around 1.6 THz) exhibits a distinct red-shift as the background refractive index (n) increases from 1 to 1.09. By tracking the shift of this specific local peak, the sensitivity of the proposed structure is calculated to be 3.3 THz/RIU

To comprehensively evaluate the sensing performance of the proposed structure, in addition to sensitivity (S), the Quality Factor (Q) and Figure of Merit (FOM) are calculated. These are standard metrics that allow for a direct comparison with other reported THz sensors. The Quality Factor represents the sharpness of the resonance peak and is defined as $Q = f_r/\text{FWHM}$, where f_r is the resonance frequency and FWHM is the full-width at half-maximum of the resonance peak. Furthermore, the Figure of Merit, which represents the overall resolution of the sensor, is defined as $\text{FOM} = S/\text{FWHM}$. For the central resonance frequency of $f_r \approx 0.99$ THz and sensitivity of $S = 3.3$ THz/RIU, the calculated values are $Q \approx 0.65$ and $\text{FOM} \approx 2.16\ \text{RIU}^{-1}$. It is worth noting that while these values are comparatively lower than those of conventional narrowband sensors, this is an inherent characteristic of broadband absorbers due to their deliberately large FWHM. The primary advantage of the proposed design lies in its ability to maintain a strong interaction with the analyte over an ultra-wide frequency range, providing dual-functionality as both an efficient broadband absorber and a reliable sensor. This relatively high sensitivity highlights the strong potential of the proposed absorber for use as an efficient refractive index sensor.

While narrowband sensors rely on tracking the shift of extremely sharp resonance peaks, the proposed broadband structure offers unique and practical advantages for sensing applications. Firstly, looking at the absorption spectra in Fig. 13, a significant variation in absorption intensity is observed in the high-frequency regime (e.g., between 1.3 THz and 1.6 THz) as the refractive index changes. For example, at $f \approx 1.35$ THz, the absorption amplitude clearly decreases from approximately 0.95 to 0.80 as n increases from 1 to 1.09. This pronounced variation enables amplitude-based sensing (intensity interrogation). From a practical standpoint, this is highly advantageous because it allows for analyte detection using a fixed-frequency THz source by simply measuring the reflected/absorbed power, thereby eliminating the need for complex and expensive wideband spectrometers.

Secondly, broadband structures exhibit much higher tolerance to manufacturing imperfections compared to ultra-narrowband designs, whose fragile resonances can be easily disrupted by fabrication errors. Finally, the proposed design offers excellent dual-functionality, serving simultaneously as a highly efficient, robust broadband absorber for electromagnetic shielding and a reliable environmental sensor.

5. Chirality analysis of the proposed graphene absorber

The chirality of the proposed broadband graphene absorber is examined through several systematic steps. From a geometrical perspective [90,91], the graphene disks are perfectly circular, ensuring complete in-plane rotational symmetry. Moreover, the graphene ribbons are straight, non-rotated, and aligned parallel to the x- and y-axes. The unit cell is periodically repeated, and there is no lateral offset or rotational misalignment between the two graphene layers. Additionally, mirror symmetry exists with respect to both the xz and yz planes. Therefore, from a purely geometrical standpoint, the proposed structure is non-chiral. The three-dimensional (stacking) chirality is also investigated. In the proposed configuration, there is no twist angle between the two graphene layers, nor is there any helical displacement or lateral offset. Furthermore, the thicknesses of the intermediate SiO_2 layers are symmetric. Consequently, the layers are fully parallel, untwisted, and non-offset, confirming that the structure is also non-chiral from a three-dimensional stacking perspective. The polarization response (TE/TM) of the absorber is then analyzed. As observed from the absorption spectra, the TE and TM curves completely overlap throughout the entire frequency range from 0 to 2 THz, i.e., $A_{TE}(f) = A_{TM}(f)$This polarization-independent response indicates that the structure does not exhibit anisotropy or magneto-electric coupling, and therefore no electromagnetic chirality is present. Next, the incident angle dependence is examined. According to the simulation results, the absorption response remains symmetric for incident angles ranging from 0° to 70°. This behavior confirms that the proposed structure functions as an angle-stable, non-chiral graphene absorber. The surface current distributions are also analyzed to further verify the absence of chirality [92]. On the graphene ribbons, the induced currents are linear, bidirectional, and symmetric with respect to the center of the structure. On the graphene disks, although circulating currents are formed, clockwise (CW) and counterclockwise (CCW) current components with equal strength coexist, resulting in a zero net circulation, $\oint J{\cdot}dl = 0$. Therefore, no chiral surface current pattern is generated. Finally, the circular dichroism (CD) is evaluated by exciting the structure with left- and right-handed circularly polarized waves. In this case, the circular dichroism is given by $CD = A_{RCP} - A_{LCP} = 0$ [93,94]. Due to the presence of mirror symmetry in the structure, the electric–magnetic coupling vanishes, leading to identical absorption responses for both polarizations. Based on all the above analyses and discussions, it can be conclusively stated that the proposed broadband graphene absorber is non-chiral.

6. Limitations and practical considerations

While this study presents a comprehensive design and analysis of the graphene-based THz absorber, it is important to acknowledge certain limitations and practical considerations. Firstly, the work relies solely on numerical simulations. Experimental validation of the proposed structure would be essential to confirm the predicted performance in a real-world scenario and to account for potential discrepancies arising from material imperfections or fabrication tolerances.

Secondly, as an inherent characteristic of broadband absorbers, the sensor performance metrics, namely the Quality Factor (Q) and Figure of Merit (FOM), are comparably lower than those typically achieved by narrowband sensors due to the significantly larger Full Width at Half Maximum (FWHM). While our design prioritizes broadband absorption and robustness, this trade-off implies that high-resolution measurements requiring extremely sharp spectral features might be more suited to narrowband approaches. However, the advantages of amplitude-based sensing and the simpler measurement setup offered by our broadband design are significant practical benefits.

Furthermore, while the proposed fabrication steps are based on standard nanofabrication techniques, achieving precise control over layer thicknesses, precise alignment, and uniformity of the graphene film across large areas can pose practical challenges in experimental realization. Future work could focus on experimental realization and addressing these fabrication aspects to fully harness the potential of this promising design.

7. Conclusion

In this work, a dual-layer broadband terahertz absorber based on graphene structures is proposed. To this end, an analytical equivalent circuit model is developed for two-dimensional arrays of graphene disks and ribbons. In addition, analytical expressions for the surface current density induced on the graphene disks and ribbons in the subwavelength regime are derived using perturbation theory under normal plane-wave illumination. The strong agreement between the full-wave simulation results and the proposed analytical model confirms the high accuracy and reliability of the developed approach. By employing a cost-function-based optimization, the parameters of the equivalent RLC circuit are optimally extracted, yielding a sum of squared errors (SSE) of 1.573. Furthermore, the proposed structure demonstrates the capability to operate as a refractive index sensor over a wide frequency range, highlighting its potential for multifunctional terahertz applications.

Declarations

The authors declare that AI tools were used to improve the English content of this paper.

Availability of data and information

All the data, designs, and relevant information associated with this paper are accessible and will be shared upon a reasonable request to the authors.

Ethical approval statement

The authors confirm that the submitted paper has not been submitted to any other journal and that this version is original and has not been published elsewhere. Additionally, all listed authors affirm the integrity of the study, data, information, and analyses, ensuring that no manipulations have been made. Furthermore, we confirm that no other individuals meet the authorship criteria for this paper beyond those listed as authors.

CRediT authorship contribution statement

Nastaran Korani: Writing – review & editing, Software, Investigation, Data curation. **Saeed Mohammadi:** Writing – review & editing, Supervision, Project administration, Formal analysis, Conceptualization. **Abdesselam Hocini:** Writing – review & editing, Supervision, Project administration, Formal analysis, Conceptualization. **Mohammad Danaie:** Writing – review & editing, Supervision, Project administration, Formal analysis, Conceptualization.

Declaration of competing interest

The authors declare that they have no known competing financial interests or personal relationships that could have appeared to influence the work reported in this paper.

Funding

The authors declare that no funds, grants, or financial support were received for the preparation of this manuscript.

References

[1] W.J. Padilla, D.N. Basov, D.R. Smith, Negative refractive index metamaterials, Mater. Today. 9 (7–8) (2006) 28–35.
[2] D.R.S.D. Schurig, J.J. Mock, D.R. Smith, Electric-field-coupled resonators for negative permittivity metamaterials, Appl. Phys. Lett. 88 (4) (2006).
[3] A.J. Danner, Visualizing invisibility: metamaterials-based optical devices in natural environments, Opt. Express. 18 (4) (2010) 3332.
[4] W. Xu, L. Xie, Y. Ying, Mechanisms and applications of terahertz metamaterial sensing: a review, Nanoscale 9 (37) (2017) 13864–13878.
[5] S. Wang, J. Du, Z. Chi, H. Cong, B. Wang, Ultra-broadband metamaterial absorber in the far infrared, Mater. Lett. 355 (2024) 135518.
[6] B. Chen, S. Yu, W. Lu, Z. Hao, Z. Yi, S. Cheng, S. Ahmad, Mid-infrared bimodal wide metamaterial absorber based on double-layer silicon nitride structure, Mater. Res. Bull. 174 (2024) 112751.
[7] S. Liang, F. Xu, H. Yang, S. Cheng, W. Yang, Z. Yi, C. Tang, Ultra long infrared metamaterial absorber with high absorption and broad band based on nano cross surrounding, Opt. Laser. Technol. 158 (2023) 108789.
[8] Y. Zhang, Z. Yi, X. Wang, P. Chu, W. Yao, Z. Zhou, Y. Yi, Dual band visible metamaterial absorbers based on four identical ring patches, Phys. E Low Dimens. Syst. Nanostruct. 127 (2021) 114526.
[9] H.F. Zhang, H.B. Liu, C.X. Hu, Z.L. Wang, A metamaterial absorber operating in the visible light band based on a cascade structure, Plasmonics 15 (6) (2020) 1755–1766.
[10] H. Xu, L. Hu, Y. Lu, J. Xu, Y. Chen, Dual-band metamaterial absorbers in the visible and near-infrared regions, J. Phys. Chem. C 123 (15) (2019) 10028–10033.
[11] M.R. Nickpay, M. Danaie, A. Shahzadi, Graphene-based tunable quad-band fan-shaped split-ring metamaterial absorber and refractive index sensor for THz spectrum, Micro Nanostruct. 173 (2023) 207473.
[12] O.M. Daraei, P. Rezaei, S.A. Khatami, P. Zamzam, S. Mohapatra, B. Appasani, S. Khani, Absorption bandwidth enhancement technique using stacked unequal cross-shaped graphene absorber, Results Opt. 21 (2025) 100872.
[13] N. Korani, S. Mohammadi, A. Hocini, M. Danaie, A terahertz tunable plasmonic absorber based on step-shaped graphene patches for sensing applications, Plasmonics (2025) 1–14.
[14] S.A. Khatami, P. Rezaei, P. Zamzam, S. Hadipour, B. Appasani, Comprehensive sensing framework for sugar molecules based on graphene absorber: coupled mode theory, transmission line analysis, and deep learning integration, Diam. Relat. Mater. 159 (2025) 112934.
[15] N. Korani, M. Danaie, A plasmonic terahertz perfect absorber based on L-shaped graphene patches and gold rods, Appl. Phys. A 129 (11) (2023) 806.
[16] N. Korani, S. Mohammadi, A. Hocini, M. Danaie, A tunable graphene dual mode absorber for efficient terahertz radiation absorption and sensing applications, Diam. Relat. Mater. 149 (2024) 111554.
[17] S.A. Khatami, P. Rezaei, M. Danaie, Performance improvement of the RI sensor based on a disk-shaped graphene absorber using pyramidal air holes in the dielectric layer, Model. Simul. Electr. Electron. Eng. (2025) 1–8.
[18] Z.W.J. Aljeboori, M.R. Malekshahi, ACOA-optimized microstrip gysel power divider with semi-radial-shaped resonators for broadband applications, Multiscale Multidiscip. Model. Exp. Des. 7 (6) (2024) 5203–5216.
[19] N. Korani, G. Hossein Roshani, F. Shama, A miniaturizing method for designing a Gysel power divider, Electromagnetics 41 (8) (2021) 594–611.
[20] M. Mohammadi, G. Karimi, H.G. Sarabi, Design of a microstrip Wilkinson power divider using a low pass filter with the particle swarm optimization algorithm, Sci. Rep. 14 (1) (2024) 17637.
[21] M. Eghballkhah, M. Hayati, F. Shama, H. Abbasi, A miniaturized modified T-shaped Gysel power divider, J. Electromagn. Waves. Appl. 39 (16) (2025) 1956–1968.
[22] S. Azami, F. Shama, M. Dousti, Ultra-wide stopband miniaturised Wilkinson power divider for application in Doherty power amplifiers, Int. J. Electron. (2025) 1–20.
[23] A. Norozi Bazaz, H. Abbasi, F. Shama, Harmonics eliminated Wilkinson power divider with modified stepped-impedance and radial units, J. Electromagn. Waves. Appl. (2025) 1–13.
[24] M.D. Fadaee, F. Shama, M.S. Feali, M.S. Gilan, A miniaturized wide stopband low-pass filter using T and modified L shapes resonators, ARO Sci. J. Koya. Univ. 11 (1) (2023) 116–120.
[25] S. Zarghami, S.A. Zonouri, S. Mehdipourbashi, A. Hatami, S.M. Shah-Ebrahimi, A high-accuracy blood glucose detection sensor using tunable bandpass filter and MLP and RBF artificial neural network algorithms, IEEE Sens. J. 24 (6) (2024) 7778–7787.
[26] S.G. Shafagh, H. Kaatuzian, M. Danaie, Design and analysis of infrared tunable all-optical filters based on plasmonic hybrid nanostructure using periodic nanohole arrays, Plasmonics 17 (2) (2022) 693–708.
[27] S. Kiani, P. Rezaei, Microwave substrate integrated waveguide resonator sensor for non-invasive monitoring of blood glucose concentration: low cost and painless tool for diabetics, Measurement 219 (2023) 113232.
[28] S. Kiani, P. Rezaei, M. Navaei, Dual-sensing and dual-frequency microwave SRR sensor for liquid samples permittivity detection, Measurement 160 (2020) 107805.
[29] S. Kiani, P. Rezaei, M. Fakhr, Dual-frequency microwave resonant sensor to detect noninvasive glucose-level changes through the fingertip, IEEE Trans. Instrum. Meas. 70 (2021) 1–8.
[30] M.R. Nickpay, M. Danaie, A. Shahzadi, Wideband rectangular double-ring nanoribbon graphene-based antenna for terahertz communications, IETE J. Res. 68 (3) (2022) 1625–1634.
[31] C. Tang, H. Cao, Q. Nie, F. Gao, J. Deng, Y. Tang, P. Gu, Graphene absorption enhancement with ultrabroad bandwidth and complete modulation near 1550 nm communication wavelength, Appl. Phys. A. 132 (1) (2026) 1.
[32] H. Cao, F. Xie, Q. Nie, C. Tang, B. Yan, F. Liu, Z. Huang, Ultra-narrowband graphene light absorption enhancement with near-perfect modulation for 1550 nm optical communication, Phys. B Condens. Matter. (2025) 418181.
[33] C. Chen, J. Liu, X. Liu, G. Liu, G. Fu, J. Chen, Z. Liu, High-performance mid-infrared fingerprint detection and solution sensing based on quasi-bound states in the continuum, Opt. Commun. 596 (2025) 132499.
[34] B. Ji, Z. Liu, Z. Lv, Q. Yang, J. Sun, G. Su, F. Liu, Targeted molecular rapid SERS diagnosis in clinical human serum through aptamer origami-collapsed nanofingers chip, Biosens. Bioelectron. 285 (2025) 117583.
[35] J.Y. Zong, M.S. Cao, Graphene-like MXene-based microwave absorbers and shields: latest progress and perspectives, Mater. Today Phys. 43 (2024) 101400.
[36] M.R. Nickpay, M. Danaie, A. Shahzadi, A wideband and polarization-insensitive graphene-based metamaterial absorber, Superlattices. Microstruct. 150 (2021) 106786.
[37] S.A. Khatami, P. Rezaei, M. Danaie, High accuracy graphene-based refractive index sensor: analytical approach, Diam. Relat. Mater. 146 (2024) 111225.
[38] N.I. Landy, S. Sajuyigbe, J.J. Mock, D.R. Smith, W.J. Padilla, Perfect metamaterial absorber, Phys. Rev. Lett. 100 (20) (2008) 207402.
[39] A.K. Geim, Graphene: status and prospects, Science 324 (5934) (2009) 1530–1534.
[40] G. Mohammadi, A.A. Orouji, M. Danaie, Highly selective single-mode graphene bandpass filter based on Wilkinson power divider structure, Diam. Relat. Mater. 145 (2024) 111141.
[41] Z. Jiang, Y. Zhang, Y.W. Tan, H.L. Stormer, P. Kim, Quantum Hall effect in graphene, Solid. State Commun. 143 (1–2) (2007) 14–19.
[42] F. Wang, Y. Zhang, C. Tian, C. Girit, A. Zettl, M. Crommie, Y.R. Shen, Gate-variable optical transitions in graphene, Science 320 (5873) (2008) 206–209.
[43] J. Kim, H. Son, D.J. Cho, B. Geng, W. Regan, S. Shi, F. Wang, Electrical control of optical plasmon resonance with graphene, Nano Lett. 12 (11) (2012) 5598–5602.
[44] X. Chen, D. Akinwande, K.J. Lee, G.F. Close, S. Yasuda, B.C. Paul, H.S.P. Wong, Fully integrated graphene and carbon nanotube interconnects for gigahertz high-speed CMOS electronics, IEEE Trans. Electron. Devices 57 (11) (2010) 3137–3143.
[45] G. Mohammadi, A. Orouji, M. Danaie, Highly compact tunable hourglass-shaped graphene band-stop filter at terahertz frequencies, Results Opt. 13 (2023) 100575.
[46] N. Korani, L. Hajshahvaladi, M. Danaie, Realization of a single-mode plasmonic bandpass filter based on a ring-shaped resonator and silver nanorods, Opt. Quantum. Electron. 56 (1) (2024) 23.
[47] N. Korani, A. Abbasi, M. Danaie, Band-pass and band-stop plasmonic filters based on Wilkinson power divider structure, Plasmonics 19 (2) (2024) 733–742.
[48] M. Kehtarmanesh, A.A. Orouji, P. Keshavarzi, M. Danaie, Design of a single-mode plasmonic bandpass filter utilizing disk and elliptic resonators in a floral configuration, Phys. Scr. 100 (5) (2025) 055539.
[49] Y. Karimi, H. Kaatuzian, A. Tooghi, M. Danaie, All-optical plasmonic switches based on Fano resonance in an X-shaped resonator coupled to parallel stubs for telecommunication applications, Optik 243 (2021) 167424.
[50] X. Dong, Y. He, R. Gao, K. Yang, J. Wang, W. Yang, Z. Yang, Plasmonic ultrafast all-optical switching with a superior on–Off ratio, Nano Lett. 25 (10) (2025) 4005–4012.
[51] J. Zun, Z. Wu, D. Fu, G. Lu, H. Hu, Novel optical switch and four-to-one data selector utilizing an MIM waveguide structure based on surface plasmon polaritons, Measurement 241 (2025) 115681.
[52] J.W. Huang, B.X. Li, C.S. Deng, High-sensitivity complex refractive index sensing using Fano resonance based on a side-coupled slotted photonic crystal nanobeam cavity, Appl. Opt. 64 (14) (2025) 4106.
[53] J. Wekalao, S.K. Patel, Design and analysis of a plasmonic metasurface-based graphene sensor for highly sensitive and label-free detection of COVID-19 biomarkers, Plasmonics 20 (4) (2025) 2109–2121.
[54] Y. Xu, S. Wu, A. Jiang, X. Liu, J. Wang, L. Shi, Self-assembly-based photonic crystal slabs for refractive index sensing via bound states in the continuum, J. Opt. 27 (11) (2025) 115102.
[55] O. Alsalman, B.B. Han, S.K. Patel, Graphene-based solar absorber structure using GaAs-Al-Zr materials for renewable energy application, Int. J. Therm. Sci. 200 (2024) 108979.
[56] S.K. Patel, B.B. Han, O. Alsalman, Solar thermal absorber design using graphene-based aluminum resonator for industrial heaters, Int. J. Therm. Sci. 201 (2024) 109000.
[57] Y. Liu, L. Hu, M. Liu, Graphene and vanadium dioxide-based terahertz absorber with switchable multifunctionality for band selection applications, Nanomaterials 14 (14) (2024) 1200.
[58] R. Rahad, A.S. Mohsin, M.B.H. Bhuian, M.M. Rahman, Graphene-metamaterial based tunable broadband polarization insensitive absorber for terahertz antenna design, IEEE Access. 12 (2024) 48654–48667.
[59] A. Zhu, P. Bu, L. Cheng, C. Hu, R. Mahapatra, High-Q multiband narrowband absorbers based on two-dimensional graphene metamaterials, in: Photonics, 11, MDPI, 2024, May, p. 469.
[60] L. He, Y. Yi, J. Zhang, X. Xu, B. Tang, G. Li, Z. Yi, A four-narrowband terahertz tunable absorber with perfect absorption and high sensitivity, Mater. Res. Bull. 170 (2024) 112572.

[61] K. Arik, S. AbdollahRamezani, A. Khavasi, Polarization insensitive and broadband terahertz absorber using graphene disks, Plasmonics 12 (2) (2017) 393–398.

[62] M. Aalizadeh, A. Khavasi, B. Butun, E. Ozbay, Large-area, cost-effective, ultra-broadband perfect absorber utilizing manganese in metal-insulator-metal structure, Sci. Rep. 8 (1) (2018) 9162.

[63] Z. Chen, P. Cai, Q. Wen, H. Chen, Y. Tang, Z. Yi, Y. Yi, Graphene multi-frequency broadband and ultra-broadband terahertz absorber based on surface plasmon resonance, Electronics 12 (12) (2023) 2655.

[64] W. Xu, S. Sonkusale, Microwave diode switchable metamaterial reflector/absorber, Appl. Phys. Lett. 103 (3) (2013).

[65] H. Wang, P. Kong, W. Cheng, W. Bao, X. Yu, L. Miao, J. Jiang, Broadband tunability of polarization-insensitive absorber based on frequency selective surface, Sci. Rep. 6 (1) (2016) 23081.

[66] F. Hu, Y. Qian, Z. Li, J. Niu, K. Nie, X. Xiong, Z. Peng, Design of a tunable terahertz narrowband metamaterial absorber based on an electrostatically actuated MEMS cantilever and split ring resonator array, J. Opt. 15 (5) (2013) 055101.

[67] J. Chen, J. Li, Q.H. Liu, Designing graphene-based absorber by using HIE-FDTD method, IEEE Trans. Antennas. Propag. 65 (4) (2017) 1896–1902.

[68] H. Wang, J. Zhu, Z. Yi, S. Cheng, J. Zhang, B. Li, A graphene-based tunable terahertz (THz) band metasurface broadband absorber under plasmon resonance effect, Solid. State Commun. 412 (2026) 116409.

[69] Z. Jin, M. Liu, S. Cheng, Z. Yi, J. Wang, B. Li, Broadband tunable metasurface absorbing device in the terahertz band based on single-layer graphene, Mod. Phys. Lett. B 40 (06) (2026) 2650017.

[70] T. Zhang, J. Zhu, Z. Yi, S. Cheng, B. Li, Tunable broadband terahertz metamaterial absorber based on graphene, Phys. Status Solidi. 263 (3) (2026) e202500573.

[71] J. Zhang, H. Niu, M. Dong, C. Gu, X. Huang, L. Qi, C. Bai, Tunable broadband terahertz absorber based on triangular-patterned graphene with sandwich configuration, in: Photonics, 13, Multidisciplinary Digital Publishing Institute, 2026, February, p. 154.

[72] L. Li, F. Chen, W. Yang, Dual-parameters tunable broadband THz absorber using hybrid graphene-Dirac Semimetal metamaterial structure, Phys. B Condens. Matter. 728 (2026) 418358.

[73] L. Li, F. Chen, W. Yang, Z. Yi, An efficient broadband absorber based on Bulk Dirac semimetal multi-trapezoidal pyramid design, Micro Nanostruct. (2025) 208408.

[74] Y. Li, F. Chen, W. Yang, A multifunctional bidirectional metamaterial perfect absorber for efficient narrowband and broadband absorption, Opt. Commun. 586 (2025) 131878.

[75] H. Fu, F. Chen, W. Yang, A broadband absorber based on W− TiO2 ellipsoidal core-shell array structure, Phys. B. Condens. Matter. 705 (2025) 417077.

[76] M. Xu, T. Liang, M. Shi, H. Chen, Graphene-like two-dimensional materials, Chem. Rev. 113 (5) (2013) 3766–3798.

[77] L. Yang, Modelling and Design of Graphene-based THz Devices (Doctoral Dissertation, Queen Mary University of London, 2019.

[78] J. Zhang, L. Zhang, W. Xu, Surface plasmon polaritons: physics and applications, J. Phys. D. Appl. Phys. 45 (11) (2012) 113001.

[79] S.A. Maier, Plasmonics: Fundamentals and Applications, 1, Springer, New York, 2007, p. 245.

[80] N. Ichiji, H. Kikuchi, M. Yessenov, K.L. Schepler, A.F. Abouraddy, A. Kubo, Observation of space-time surface plasmon polaritons, Nat. Commun. 16 (1) (2025) 10697.

[81] W.S. Weiglhofer, Analytic methods and free-space dyadic Green's functions, Radio Sci. 28 (05) (1993) 847–857.

[82] A. Khavasi, B. Rejaei, Analytical modeling of graphene ribbons as optical circuit elements, IEEE J. Quantum. Electron. 50 (6) (2014) 397–403.

[83] S. Barzegar-Parizi, B. Rejaei, A. Khavasi, Analytical circuit model for periodic arrays of graphene disks, IEEE J. Quantum. Electron. 51 (9) (2015) 1–7.

[84] S. Barzegar-Parizi, B. Rejaei, A. Khavasi, Analytical circuit model for periodic arrays of graphene disks, IEEE J. Quantum. Electron. 51 (9) (2015) 1–7.

[85] N. Rouhi, S. Capdevila, D. Jain, K. Zand, Y.Y. Wang, E. Brown, P. Burke, Terahertz graphene optics, Nano Res. 5 (10) (2012) 667–678.

[86] G.W. Hanson, Dyadic Green's functions for an anisotropic, non-local model of biased graphene, IEEE Trans. Antennas. Propag. 56 (3) (2008) 747–757.

[87] E. Forati, G.W. Hanson, Soft-boundary graphene nanoribbon formed by a graphene sheet above a perturbed ground plane: conductivity profile and SPP modal current distribution, J. Opt. 15 (11) (2013) 114006.

[88] K. Arik, S. AbdollahRamezani, A. Khavasi, Polarization insensitive and broadband terahertz absorber using graphene disks, Plasmonics 12 (2) (2017) 393–398.

[89] H. Fu, F. Chen, Dual-narrowband terahertz absorber with independently tunable amplitude and frequency: a theoretical study, Phys. Lett. A 574 (2026) 131395.

[90] Lindell, I.V., Sihvola, A.H., Tretyakov, S.A., & Viitanen, A.J. (1994). Electromagnetic waves in chiral and bi-isotropic media.

[91] J. Pendry, A chiral route to negative refraction, Science 306 (5700) (2004) 1353–1355.

[92] U.U.R. Qureshi, B. Hu, M. Ahmad, A. Jalal, Graphene-based triple-band tunable metasurface with strong circular dichroism for THz communication, IEEE Photonics. Technol. Lett. 35 (24) (2023) 1375–1378.

[93] Y. Tang, A.E. Cohen, Optical chirality and its interaction with matter, Phys. Rev. Lett. 104 (16) (2010) 163901.

[94] L.D. Barron, Molecular Light Scattering and Optical Activity, Cambridge University Press, 2009.